POLITECNICO
MILANO 1863

SCUOLA DI INGEGNERIA INDUSTRIALE
E DELL'INFORMAZIONE

Ultrafast Terahertz Spectroscopy of Trilayer MoS_2

Tesi di Laurea Magistrale in
Engineering Physics - Ingegneria Fisica

Author: **Federico Grandi**

Student ID: 971130
Advisor: Prof. Salvatore Stagira
Co-advisors: Eugenio Cinquanta, Caterina Vozzi
Academic Year: 2021-22

Abstract

Transition metal dichalcogenides are a family of low-dimensional materials that gained importance as they can be exploited in electronics and optics thanks to their peculiar physical properties. MoS_2 received particular attention given its availability in nature as a bulk crystal and its interesting effects linked with its excitonic population and band-gap properties. In this thesis, we will exploit ultrafast THz spectroscopy to investigate low-energy vibrational modes arising from the relative motion of the layered structure of a few layer sample of MoS_2. Despite these modes have been predicted and observed via Raman spectroscopy there are yet no observations performed in the THz frequency domain. In particular both with static and pump-probe measurements we will try first to identify the presence of these phonon modes and then to investigate how they interact and couple with the free carriers due to excitation of the sample.

Keywords: TMDs, MoS2, THz spectroscopy, charge-phonon coupling

Abstract in lingua italiana

I dicalcogenuri dei metalli di transizione sono una famiglia di materiali a bassa dimensionalità che hanno ottenuto una grande importanza grazie alle loro particolari proprietà fisiche, in particolare nei campi dell'elettronica e dell'ottica. Tra questi il MoS_2 ha ricevuto particolare attenzione grazie anche alla sua presenza in natura sotto forma di minerale e alle proprietà derivanti dalla sua popolazione di eccitoni e proprietà del suo gap energetico. In questa tesi verrà utilizzata la spettroscopia THz ultraveloce per investigare i modi vibrazionali a bassa energia derivanti dal moto relativo dei layer che compongono la struttura di un campione di MoS_2 a bassa dimensionalità. Malgrado questi modi siano già stati predetti e poi osservati grazie alla spettroscopia Raman, non vi sono ancora osservazioni dirette effettuate nell'intervallo spettrale del THz. In particolare, attraverso acquisizioni statiche e di pump-probe si tenterà di identificare la presenza di questi modi e successivamente si cercherà di comprendere come questi interagiscono e si accoppiano con cariche libere derivanti dall'eccitazione del campione.

Parole chiave: TMDs, MoS2, Spettroscopia THz, accoppiamento carica-fonone

Contents

1 | Introduction

1.1. 2D Materials

In the past two decades, the interest in nanomaterials has grown significantly, with the aim of finding new alternative materials to enhance or even substitute existing technologies. The discovery of graphene in 2004 by Novoselov and Geim [1] was the first breakthrough in the realm of two-dimensional materials and for this reason, lead its discoverers to a Nobel prize in 2010. Graphene is a 2-dimensional layer of carbon atoms arranged in a hexagonal lattice that can be extracted both by a bulk sample of graphite or grown on specific substrates, and is still nowadays the most known and studied example of low-dimensional material. After this first discovery, material scientists never stopped looking for new compounds and materials with more peculiar properties.

Nowadays the category of 2D materials includes several examples, apart from the already presented graphene, other compounds part of this family are hexagonal boron nitride (h-BN), transition metal dichalcogenides (TMDs), 2D perovskites, and even more, considering also the heterostructures arising from the staking of different layers of these materials. In particular, h-BN is, after graphene, one of the most studied 2D material, with good applications in the fabrication of very high-quality substrates and insulators. TMDs are semiconductors composed of a chalcogen, an atom of the sixth group of the periodic table, and a transition metal element in a layered structure, while perovskite seems to be the next breakthrough in solar energy harvesting and are more complex compounds defined by a particular elementary cell's structure.

The main feature of these kinds of materials arises from their geometrical structure, and in particular from their dimensionality. Because of this, all two-dimensional materials comes with a very high specific surface area with respect to their bulk counterpart. Other than that, depending on the specific material, other exotic properties arise, with promising high potentiality in several scientific and technical fields like electronics, optics, chemistry, and engineering in general.

Their atomic structure allows for good mechanical properties under stress, with high

breaking strength and elasticity with respect to commonly used bulk materials. Electrically speaking, these materials show a vast variety of behavior; starting from graphene which presents very high charge conductivity given by its peculiar band structure, h-BN, on the other hand, behaves like an insulator while TMDs are semiconductors. On the optical side, their low dimensionality allows reaching very high optical transmittance, that together with their band-gap properties allows for interesting applications in optics. It is then possible to exploit them also in chemistry, where they could be applied as catalysts or in purification systems [2].

Fabrication of these materials may vary depending on the overall desired quality. The first method discovered involved mechanical exfoliation of the single layers from a bulk sample, which require the use of physical tools to separate each layer from the others. More advanced techniques involve the use of liquid [3] and chemicals to perform an effective exfoliation in a top-down approach, or the growth of the sample both with chemical or physical vapor deposition of the material in a bottom-up approach.

Many applications exploit the peculiarity of these materials in specific devices. Starting from electronics it is possible to apply these materials in field effect transistors [4] and in non-volatile memories [5]. The possibility of tuning the band-gap acting on the staking of different layers opened the field of optical application both in sensors for detection and emission devices [6][7]. Another class of 2D materials, 2D van der Waals magnets, showed promising application in the field of magnetism and spintronics [8]. Combining structural strength and electrical properties 2D materials are also good candidates for the energy harvesting industry, especially with solar cells and batteries.

To enable a deep understanding of these new materials it is then necessary to use a suitable investigative method able to gather information about the fundamental physics behind their properties. Light can be exploited exactly for this purpose, and in particular ultrafast spectroscopy techniques have become the principal characterization method for this kind of analysis, given their capabilities of observing these phenomena with very high detail and precision.

1.1.1. TMDs

In this thesis, the focus will be on TMDs and in particular on MoS_2 . TMDs are a big family of materials, that can be stripped down to a 2-dimensional configuration. Their structure has been proposed for the first time by Linus Pauling in 1923 [9] and the first two-dimensional mono-layer sample is dated back in 1986 [10]. Their structure is in the form of MX_2 where M is a transition metal and X is a chalcogen atom. A bulk TMD

is composed of a stack of layers held together by weak van der Waals forces, which can then be exfoliated in order to obtain a few- to mono-layer configuration. The particular peculiarity of this family of materials is the behavior of their band-gap. By reducing the layer count from few- to mono-layer it is possible to observe a shift from an indirect band-gap to a direct one, resulting also in changes in the optical property of the sample, like increased absorption and photoluminescence [11].

MoS_2 is probably one of the most famous instances of this category given its availability in nature as a crystal and has been studied since the '60 for a variety of applications. The low dimensionality determines a reduced screening of the electron-electron Coulomb interaction inside the material that together with quantum confinement results in a large exciton binding energy [12]. Another result is the formation of excitation such as trions, already observed for MoS_2 [13]. Ultrafast spectroscopy both in the visible and near-infrared allowed the observation of these phenomena together with the strong electron-phonon interaction and non-linear optical processes.

1.1.2. THz spectroscopy of TMDs

Considering the feature of TMDs proposed up to now, it is possible to exploit THz ultrafast spectroscopy to investigate and interact with the phenomena that characterize this family of materials. THz radiation is able to interact with several low-energy excitations of the electronic structure of materials. In particular THz radiation is highly interacting with free charges, electron-phonon interaction, and all the low energy collective phenomena involving charges [14]. The information retrieved by this light-matter interaction allows the investigation of transport phenomena of carriers, together with the possibility of retrieving the complex conductivity of samples detecting at the same time both amplitude and phase information. Combining the use of THz radiation with ultrafast laser sources it is then possible to follow these phenomena with a very high temporal sensitivity, becoming able to fully observe the dynamic of the physical phenomena governing such low-dimensional materials.

Regarding the use of this technique for TMDs it is possible to infer about charges, excitons, and trions dynamics, allowing also to analyze how different fabrication techniques could lead to different behaviors. In MoS_2 this technique allowed to analyze charged carriers and obtain indirect measures of the presence of the rich exciton population predicted by other investigation techniques [15]. Recombination dynamics have been also investigated, leading to the discovery that relaxation kinetics is highly dependent on defect states, which vary also depending on the number of layers of the structure [16]. Despite the presence

of low-energy vibrational modes arising from the relative motion of the layers observed with Raman spectroscopy and predicted by first-principles calculations [17], there is yet no direct observation with THz spectroscopy. In the following chapters, effects arising from the presence of these phonon modes and their interaction with free charges will be investigated.

2 | Methods

This chapter will analyze the theoretical and technological background necessary to understand how a THz time-domain spectroscopy experiment is carried out. At first generation and detection schemes for THz radiation will be reviewed, then the experimental setup used for the experiment will be presented. Finally, there will be a brief description of the experimental techniques that is possible to perform on samples, together with the theoretical models applied for data analysis.

2.1. THz Generation

There are several ways to generate THz pulses for spectroscopic purposes, but all of them require the usage of a femtosecond laser oscillator generally with a subsequent amplification system. These methods can be divided into two main categories depending on the underlining physical processes exploited: photoconductive antennas and generation through non-linear optical effects [18].

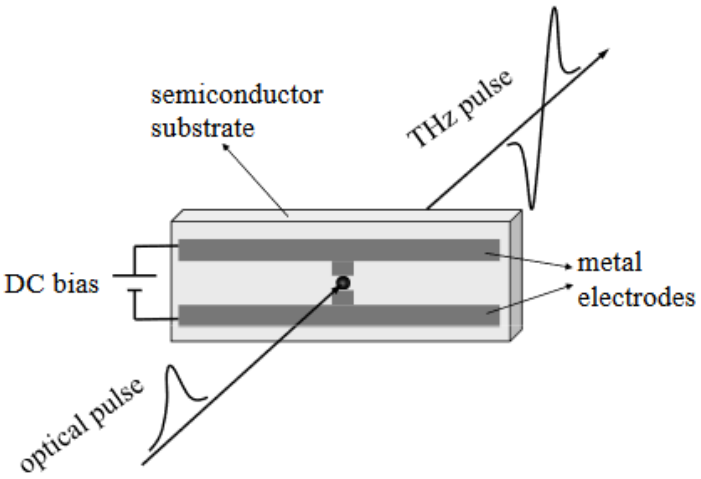

Figure 2.1: General schematic of THz generation with a PCA [19]

Photoconductive antennas (PCA) generally do not require the use of an amplified system

and are composed of two metal contacts, the dipole antenna, fabricated via lithography on a photoconductive substrate made out of an intrinsic semiconductor and biased with a strong DC field. The driver femtosecond pulse is absorbed by the gap between the two metal contacts, and excites charge carriers in the conduction band, generating a photocurrent which can be evaluated as the convolution between the optical pulse and the impulse response of the semiconductor:

$$I_{PC} \propto \int I_{opt}(t - t')[en(t')v(t')]\, dt' \tag{2.1}$$

with I_{opt} intensity of the laser pulse and $n(t)$ and $v(t)$ carrier density and average electron velocity in the substrate [19].

It can be shown [19] that this current drives the THz generation by inducing a dipole moment in the gap of the antenna. The emitted field at a distance r and at an angle α can be written as:

$$E_{THz}(t) \propto \frac{sin(\alpha)}{r} \frac{dI_{PC}(t)}{dt} \tag{2.2}$$

Proportional to the derivative of the generated photocurrent.

Regarding the bandwidth of the generated pulses, the limiting factors in PCA arise from the lifetime of the generated photocarriers: with a long recombination time, the photocurrent will switch off much later than the driver pulse absorption, leading to a broadening of the THz pulse duration with a reduction in bandwidth [20]. Moreover, it is possible to reduce the bandwidth narrowing by tuning the size of the emitting antenna at dimensions smaller than the emission wavelength [21].

Another approach for the generation of ultrafast THz pulses employs non-linear optical effects due to the interaction of a high-intensity ultrashort pulse with a suitable crystal. This generation method was first demonstrated in 1965 by Zernike and Berman by using quartz and obtaining frequencies in the near-infrared[22].

Dealing with crystals, the main non-linear effect generating the THz field is a second-order effect: optical rectification. For this reason, the symmetry of the crystal plays an important role as second-order non-linear effects arise only with noncentrosymmetric media. Let us start now with a brief description of optical rectification starting from the relation between polarization and electric field in linear conditions:

$$P = \epsilon_0 \chi(E) E \tag{2.3}$$

where $\chi(E)$ is the electric susceptibility of the considered medium. By expanding this term in power of the field E is now possible to study how the interaction with a stronger electric field arises contributions other than the linear one:

$$P = \epsilon_0(\chi_1 + \chi_2 E + \chi_3 E^2 + \chi_4 E^3 + ...)E \tag{2.4}$$

As already said, for the purpose of THz generation, we are interested in a second-order non-linear process as it is the main contributor to this effect, so we deal now with the $P_2^{NL} = \epsilon_0 \chi_2 E^2$ term. Consider now, for example, an electric field in the form: $E = E_0 cos(\omega t)$, and by plugging it in the non-linear polarization term we get:

$$P_2^{NL} = \epsilon_0 \chi_2 E^2 = \epsilon_0 \chi_2 \frac{E_0^2}{2}(1 + cos(2\omega t)) \tag{2.5}$$

Here, is clear how the second-order electrical susceptibility gives two polarization contributions, a continuous component and another one at frequency 2ω; we will call the first optical rectification and the second second-harmonic generation. It is possible now to perform the same calculation considering the interaction between two different components at different frequencies $E_1 = E_0 cos(\omega_1 t)$ and $E_2 = E_0 cos(\omega_2 t)$:

$$P_2^{NL} = \epsilon_0 \chi_2 E_1 E_2 = \epsilon_0 \chi_2 \frac{E_0}{2}[cos(\omega_1 - \omega_2)t + cos(\omega_1 + \omega_2)t] \tag{2.6}$$

with two terms arising from the frequency mixing of the two interacting fields, one oscillating at the difference of the frequencies and one at the sum. THz generation relies on the first term, the difference frequency polarization arising from the mixing of all the frequencies in the bandwidth $\Delta\omega$ of the femtosecond laser pulse [23].

Regarding the spectral width of the generated THz pulse, the main aspects to consider are the phonon resonances in the crystal, which introduce absorbance on the emitted spectrum, and the phase matching condition between the near-IR and THz pulse. While phonons inside the material are impossible to avoid, phase matching can be tuned in order to find an optimal configuration. Generally, the phases of the fields arising in different positions of the crystal from the interaction with the laser pulse lead to a cumulative destructive interference that dumps the generated THz wave. On the other hand, under particular conditions it is possible to achieve constructive interference between all the different oscillators inside the material, this happens when we achieve phase matching conditions. The requirement is that the wave vector of the THz field ought to be equal to the difference of the wave vectors of the frequencies of the mix:

$$k_3(\Omega) = k_1(\omega_1) - k_2(\omega_2) \tag{2.7}$$

and so

$$\Omega n_3(\Omega) = \omega_1 n_1(\omega_1) - \omega_2 n_2(\omega_2) \tag{2.8}$$

with n_i refracting index of the i-th component depending on the frequency and on the polarization for a birefringent media [24]. Supposing to obtain phase matching conditions on all possible components of the laser spectrum, the bandwidth of the THz pulse will then only be limited by the spectral width of the laser pulse itself. But that's not achievable and thus each crystal achieves optimal generation at a different wavelength [19].

A popular crystal choice for THz generation with optical rectification is ZnTe which can be pumped with the 800 nm generated by a common Ti:Sa laser, its electrical susceptibility is high and it allows THz bandwidth up to 3 THz. Another commonly used crystal is GaP which offers bandwidth up to 7 THz due to its phonon resonances located at higher frequencies with respect to ZnTe [25]. For a more broadband generation, GaSe crystals or organic crystals are also used as they can be tuned at even higher frequencies up to 100 THz [26] for the first, under suitable phase matching conditions, and 180 THz for the second [27], but for the latter reliability may be an issue [28].

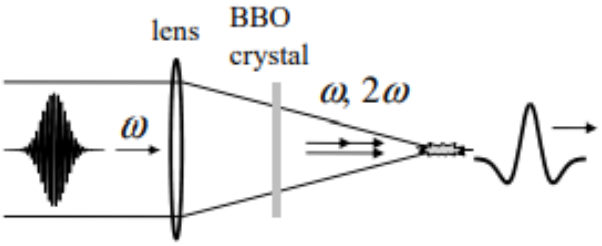

Figure 2.2: General schematic of THz generation with laser-induced air plasma [19]

Yet another possible method exploitable for THz generation is laser-induced air plasma, first demonstrated by Cook and Hochstrasser in 2000 [29]. In this case, the interaction happens between the fundamental wave of the laser and its second harmonic forming a two-color electric field that is focused to generate a plasma. Physically, the asymmetric two-color field ionizes the bound electrons of the air molecules which oscillate with a time scale comparable with the photoionization, emitting THz radiation [30].

For instance, the THz pulse is proportional to the time derivate of the nonlinear current:

$$E_{THz} \propto \frac{\partial}{\partial t} J^{(3)}(t) \tag{2.9}$$

where

$$J^{(3)} = \sigma^{(3)} E_{2\omega} E_{\omega} E_{\omega} e^{-i\phi} \tag{2.10}$$

with $\sigma^{(3)}$ nonlinear conductivity and ϕ phase difference between the two colors [19]. Also in this case the polarization of the incident waves is important for the resulting efficiency of the process and for the resulting polarization of the THz field. Finally, it is possible to further improve generation performance by acting on the gas and pressure in which plasma is generated [24]. The bandwidth of the resulting THz pulses is generally very broad up to the near-infrared [31].

2.2. THz Detection

Also for detection, it is possible to exploit several methods that can be divided mainly into two big categories: incoherent and coherent detectors.

An incoherent detector is generally a broadband detector able to directly retrieve only intensity information of the impinging THz field, the most common devices in this category are bolometers and Golay cells. Despite their simplicity, they are generally not deployed in spectroscopy setups as there exist other methods more suitable for the extraction of all the relevant information needed for a time-domain experiment.

On the other hand, coherent detectors allow for the retrieval of both amplitude and phase information of the received THz pulse allowing for a full reconstruction of the complex response of materials without the need for the Kramers-Kronig relations. These kinds of detectors work in a heterodyne configuration as they need to downconvert the frequency of the detected pulse allowing the electronic circuit to measure it [32]. In this case, the technologies used for detection exploit roughly the same effects used for THz pulse generation.

Photoconductive antennas work with the same principle of generation but this time do not require the external bias voltage which is substituted by the transient electric field of the THz pulse. The generated potential between the contacts interacts with the charge carriers coming from the interaction of the laser pulse with the semiconductor substrate. The generated current is then measured for the reconstruction of the THz pulse by varying

the time delay between the THz pulse and the femtosecond probing laser pulse which will be called gate pulse later on in this discussion. The bandwidth of PCA detectors depends on the response function of the device and in particular on the pulse length of the laser and the carrier lifetime in the semiconductor [19].

Detection with a crystal exploits the so-called electro-optic or Pockels effect in which the incoming THz pulse introduces a phase change in an interrogating femtosecond laser pulse by interacting with the detecting media. The probing laser pulse, due to its time duration, sees the THz field as a constant one so that it is possible to reconstruct all the THz waves by changing the time delay between the two. The phase change is in the form of a birefringence induced by the THz pulse acting on the laser pulse's polarization components which is no more linear as a result.

This effect is closely related to the optical rectification described previously for generation: it is a second-order non-linear process exploiting the same term in the susceptibility tensor of the detecting material. The detection scheme with electro-optic sampling require more component than just the EO crystal: in order to measure the polarization changes on the laser pulse, the EO crystal is followed by a $\frac{\lambda}{4}$ waveplate, a Wollaston prism and finally two photodiodes. The laser pulse arrives with a linear polarization on the detection crystal, here the birefringence induced by the THz pulse introduces a change in polarization due to the different refracting indices the pulse crosses while in the material. The $\frac{\lambda}{4}$ waveplate, introduce then a $\frac{\pi}{2}$ phase shift to one component of the pulse which becomes now elliptically polarized. Finally, the Wollaston prism separates the two polarization components which are then measured by two photodiodes. The signal is the difference between the two signals. Supposing no THz field is present, the detection crystal behaves like an isotropic media with no change induced on the probing laser pulse and the quarter waveplate is rotated so that the output pulse is circularly polarized, thus resulting in a zero difference signal. On the other hand, if the detection crystal introduces a phase change in one polarization direction the resulting field after the waveplate would not be circularly polarized but elliptically and so a difference in the signal on the two photodiodes will be measured. An important aspect of EO detection is to tune the waveplate orientation in order to obtain zero signal when no THz pulse is present [33].

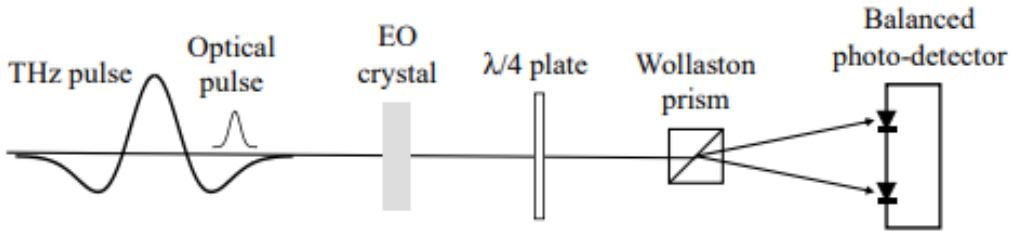

Figure 2.3: General schematic of THz detection with EO sampling on a crystal [19]

2.3. Experimental Setup

2.3.1. Laser

An important part of the experimental setup is the laser system. In the laboratory this is a Ti:Sa amplified laser system, in order to achieve pulses of roughly 25 fs with a repetition rate of 1 kHz at 790 nm with a bandwidth of 80 nm. After the oscillator, the pulses are amplified with the CPA technique (Chirped Pulse Amplification). This technique was first proposed by Mourou and Strickland in the mid-1980s and allowed to reach high-intensity ultrashort pulses with a reduced risk of damaging the amplification system.

The process is composed of three main stages: stretching, amplification, and compression. First, a weak ultrashort laser pulse generated by an oscillator operated in mode locking is stretched with a particular configuration of gratings that introduce a chirp which broadens the time duration of the pulse up to hundreds of picoseconds. Then the pulse undergoes an improvement in quality given by a suitable acousto-optic programmable dispersive filter (AOPDF), necessary to compensate for temporal distortions in the pulses.

Then the actual amplification process takes place, involving three steps: regenerative amplification and two multipass amplifications. The first stage exploits a Pockels cell to trap the pulse in a laser cavity where the pulse is amplified by performing multiple round trips through a Ti:Sa crystal pumped with Q-switched Nd:YLF lasers at 532nm. When the amplification in the cavity reaches saturation the pulse is extracted by another Pockels cell and sent to the other amplification stages. Inside the regenerative amplifier's cavity an acousto-optic programmable gain control filter (AOPGCF) optimizes the bandwidth of the pulse with the aim of achieving a top hat spectral profile with the desired bandwidth and central frequency.

The final amplifications stages are multipass amplifiers where the pulse performs some

passages in a Ti:Sa crystal also pumped with Q-Switching Nd:YLF lasers with the crystal of the second multipass held under cryogenic temperature in a cryostat. Now the pulse is able to reach an energy of roughly 17 mJ. Subsequently, the laser beam is split between the different experiment present in the laboratory and the THz spectroscopy setup use about 1.5 mJ of the total energy available. Before the actual setup the last stage of CPA, compression, takes place. Using other gratings the chirp introduced by the stretcher is compensated allowing to restore the transform-limited condition. Actually, it has been found that the optimal condition for THz generation in thick ZnTe crystals requires some negative chirping of the laser pulse in order to compensate for dispersion [34].

2.3.2. THz spectrometer

As soon as the pulse is compressed it enters the actual experimental setup. First, the beam encounters two beam splitters which divide the three pulses needed for a time-resolved THz spectroscopy experiment: the pulse needed for THz generation, the pump pulse needed for the photoexcitation of the sample, and the pulse needed for detection with electro-optic sampling which will be called gate pulse from now on. After the beam splitters, the generation and pump beam are modulated with a chopper with two different modulation frequencies necessary for the lock-in detection and amplification in a technique called double demodulation which will be explained later on. Now, we will follow the path of the three beams across the setup starting from generation. After the modulation, the generation pulse enters an externally controlled delay stage which is able to introduce a time delay with respect to the gate pulse. This time delay is fundamental for the THz wave detection as it allows the ultrafast gate pulse to probe different parts of the way longer THz pulse to reconstruct its shape in the temporal domain. The generation beam then enters the experimental chamber, a small box containing the sample and the actual THz generation and detection stage. This enclosure is necessary because the THz radiation is damped by water vapor in the atmosphere and thus it is necessary to perform the actual experiment in a water-free area. To get this condition the experimental chamber is fluxed with nitrogen for the whole experiment duration. After entering the chamber the generation pulse is focused with a spherical mirror in the 1mm-thick ZnTe crystal with <110> orientation for phase matching purposes. Here the optical rectification process turns part of the IR pulse into THz radiation which is collected by an off-axis parabolic (OAP) gold-coated mirror. The configuration of the gold-coated parabolic mirrors allows to focus the beam after two reflections onto the sample. After the interaction, the THz wave is recollected by two other parabolic mirrors which further focus the beam on the ZnTe detection crystal for the electro-optic sampling.

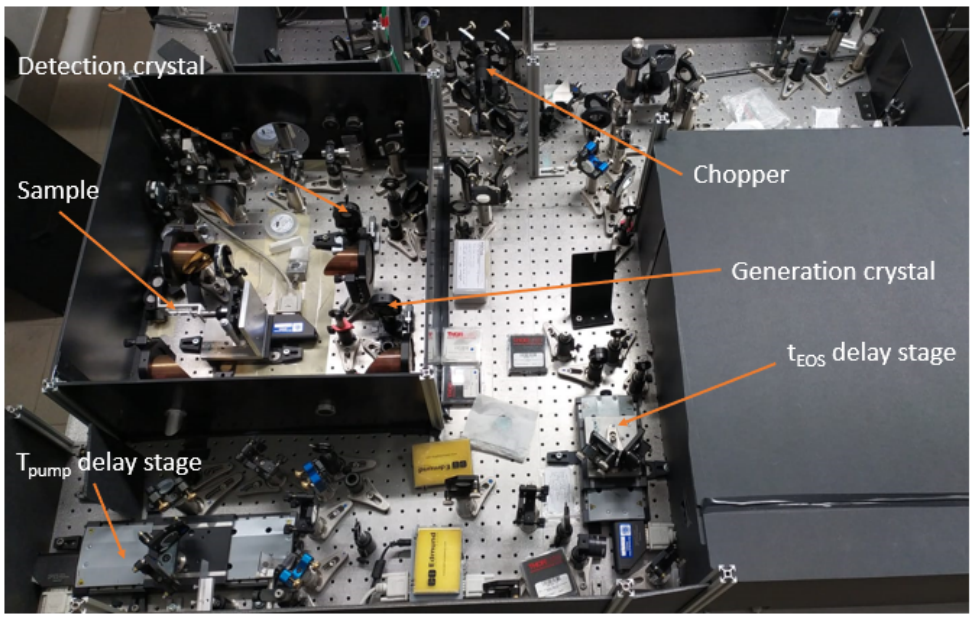

Figure 2.4: Photo of the THz spectrometer at the UDynI laboratory at Politecnico di Milano

The gate pulse allows the system to retrieve the THz electric field by sensing the birefringence induced on the detection crystal. The gate pulse enters the experimental chamber through a window and, by passing through the THz parabolic mirrors, ends up collinear with respect to the THz wave, in this condition it impinges on the ZnTe detection crystal. After the interaction via the electro-optic effect, it exits the chamber, passes through a $\frac{\lambda}{4}$ waveplate and a Wollaston prism so that the two components of the now circularly polarized wave are separated and then detected by two photodiodes.

Finally, the modulated pump pulse enters another delay stage which introduces the delay between pump and probe beam, necessary to perform pump-robe experiments. After that, the beam is focused with a spherical mirror to increase the fluence on the sample. Before entering the experimental chamber for the purposes of this experiment a BBO crystal is used in order to get the second harmonic of the 800 nm pulse which is then removed with a colored glass filter. A Brewster's angle window is located at the entrance of the experimental chamber. Here the pump beam passing through a parabola becomes collinear with the THz one and in this condition we get a focusing of both beams on the sample. In order to discard all the pump photons after the interaction, a high-density polymer filter which is transparent to THz radiation, but absorbs in the UV-IR region, is placed right after the sample. Such a filter is necessary as it avoids unwanted interaction of the pump beam with the optical elements further on in the line.

A key point in the setup is the optimization required to get the best signal possible. The

main procedure that has to be verified day by day is the spatial overlap between pump and THz and THz and gate. First, we tune the interaction between the pump and probe pulse on the sample. In order to get the maximum available signal out of the pump-probe experiment, the two pulses have to be well spatially overlapped so that the probe THz pulse is able to interact with a fully photoexcited region. In order to get such optimal overlap, a known sample was used as a reference so that by moving the last mirrors of the pump before the interaction, it was possible to maximize the pump-probe signal. Second, it is the turn of the spatial overlap between THz and gate pulse needed to obtain the higher possible signal out of the detection crystal. In this case, the optimization procedure was performed by tuning the parabolic mirror of the THz line while measuring the signal out of the setup in order to maximize it.

2.4. Data acquisition and analysis

A crucial part of THz detection is the ability to measure and amplify very small signal differences while maintaining a good signal-to-noise ratio. The device commonly adopted for such purposes is the lock-in amplifier.

The working principle of this kind of amplifier relies on a homodyne detector and a low-pass filter to extract signals around a specific reference frequency rejecting all other components.

The signal to be measured, a train of laser pulses, is first modulated at a reference frequency with an optical chopper or an acousto-optic modulator. This same reference signal act as a trigger for the demodulation stage in the lock-in amplifier. The modulated train can then propagate in the setup acquiring the information relevant to the experiment and ending up in the actual lock-in device. Here the signal is multiplied by the same reference performing a demodulation process, the resulting signal is then filtered with a low pass filter so that only the relevant information encoded at a specific frequency can be recovered rejecting all the non-modulated noise [35].

In order to achieve this behavior, it is important that the modulation is performed as soon as possible in the setup to avoid the noise introduced later on by the propagation.

During a pump-probe experiment, the measured signal represents the relative difference between two states of the sample: the photoexcited and the non-photoexcited state. This kind of measurement requires to perform two different acquisitions, one with the pump blocked and one with the pump free to propagate. In such a case, apart from the time required to perform both the acquisition instead of one, there is also the risk of incurring

in changes in the laser conditions during this time span leading to higher noise and errors in the data. The double demodulation technique allows to overcome both these issues allowing for faster scans and reducing the risk of error together with the overall noise reduction on the measurement. The technique is based on the modulation of both generation and pump beam with different frequencies prime one to the other, performed with a mechanical chopper composed of two sets of slits at different periodicity. This signal is then made to interact with the sample and is finally collected by two independent demodulators at the respective frequencies from which is then possible to extract the actual pump-probe trace.

A simple demonstration to better grasp this concept can be done by supposing a modulation of 500 Hz on the pump beam and of 333 Hz on THz generation with a laser repetition rate of 1kHz. Important to notice that in order to avoid cross-talk between the two beams the modulation frequencies are not harmonic to one of the other.

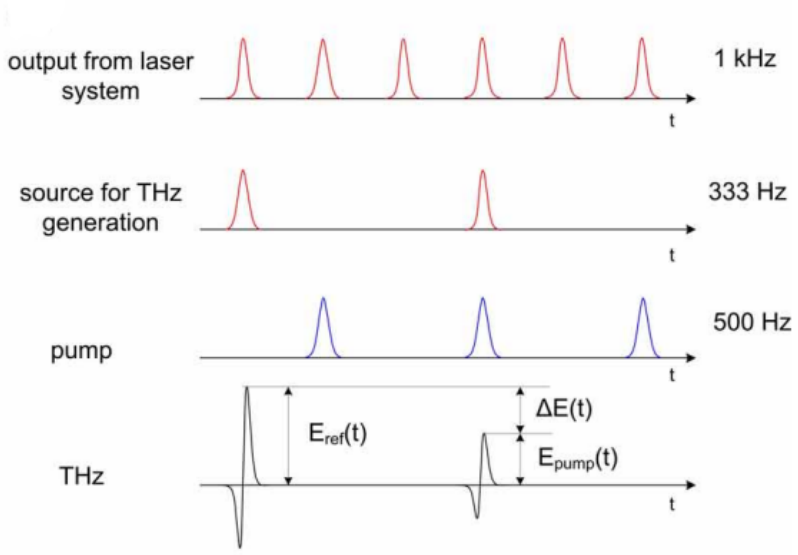

Figure 2.5: Schematic of double demodulation technique for pump-probe measure [36]

As shown in figure 2.5, with such modulation frequencies it is possible to acquire, with a single measurement, both the THz wave with pump interaction and without, by demodulating the photodiodes signals with two different demodulators at the respective trigger frequencies. The measured field by the two photodetectors would then be:

$$E_1(t) = \frac{E_{ref}(t) + E_{pump}(t)}{2} \tag{2.11}$$

$$E_2(t) = \frac{E_{ref}(t) - E_{pump}(t)}{2A} \tag{2.12}$$

Where E_{ref} reference field without pump, E_{pump} field with pump interaction, and A calibration constant due to the response of the photodiodes [36].

2.4.1. Bandwidth and resolution of the THz spectrometer

A time-domain measurement is performed by spanning a time window centered on the peak of the THz field with a suitable time resolution. This resolution must be chosen as a tradeoff between the time duration of a single scan and the bandwidth requirement of the generation and detection crystal used. ZnTe crystals allow for a spectral width of about 3 THz, by exploiting the Nyquist-Shannon theorem it is possible to derive the minimum sampling frequency, f_s required to acquire a 3 THz signal:

$$f_s > 2f_M = 6\ THz = 6 \cdot 10^{12}\ Hz \tag{2.13}$$

from which is then possible to derive the maximum time resolution, δt of such sampling:

$$\delta t \leq \frac{1}{f_s} = \frac{1}{6 \cdot 10^{12}\ Hz} \simeq 167\ fs \tag{2.14}$$

Therefore, with ZnTe as the generation crystal, a time resolution of 100 fs is good enough to sample the THz electric field avoiding aliasing artifacts.

Concerning the spectral resolution, it is related to the total time span of the measurement, Δt. For example, if one acquires the THz electric field in the time-domain from -2 ps to 4 ps ($\Delta t = 6$ ps), the spectral resolution of the measurements is defined as follows :

$$d\nu = \frac{1}{\Delta t} = 160\ GHz \tag{2.15}$$

Theoretically, the sharpest resolvable spectral feature could be infinitesimally small supposing an arbitrarily large time window. In practice, this is not true, as the real measurement is affected by noise which reduces the maximum available resolution.

2.4.2. THz measurements

Static measures are the simpler kind of measure we can perform on a sample, they require no pump pulses and exploits only the interaction of the THz pulse with the

material. As presented before in section 2.2, to acquire the THz wave with EOS it is necessary to work with the THz-gate delay t_{EOS}.

The aim of a static measure is to evaluate the static complex transmission of the sample from which it is then possible to retrieve its dielectric function. This response is fundamental to investigate the static properties of the material as THz waves interact strongly with free charges and phonons inside the materials. The measure, in this case, supposes a differential approach in which each scan of the material ought to be paired with a reference scan of the substrate alone or of the air in the experimental chamber thanks to which is then possible to retrieve only the material transmission neglecting the effect of the other components and materials inside the chamber.

Pump-probe measurements can be further divided into two subcategories depending on the value of t_{EOS} applied:

- 1D dynamics
- 2D maps

1D dynamics measurement are made fixing t_{EOS} at a specific point of the THz pulse, generally the maximum amplitude point, and then performing a measurement varying the pump delay with respect to the THz pulse, t_{pump}. This kind of measurement follows the evolution of the dynamics of the photoexcitation process of a particular material, starting from negative delays, where no signal is expected, and going on generally until the observed signal is completely dumped. From dynamic measurements, the main information retrieved is about electron mobility in the material and the decay channels that the generated photocarriers undergo while recombining. Following the decay curve, is possible to model and fit the various time constants of the physical phenomena governing the relaxation of the material after the interaction with the pump pulse.

This kind of measurement exploits the use of a double demodulation technique to measure simultaneously both the differential and the reference signal.

2D maps are the actual full pump-probe measurements that it is possible to perform on the setup, here both t_{EOS} and t_{pump} change generating a 2D map of the response of the material with respect to the THz and pump wave. Because of the demodulation process involved in the acquisition procedure the measured signals out of the setup are the difference between photoexcited and not photoexcited THz field $\Delta E = E_{on} - E_{off}$ and the reference field E_{off}. The differential transmission is then:

$$\frac{\Delta T}{T} = \frac{E_{on}}{E_{off}} = \frac{\Delta E}{E_{off}} + 1 \tag{2.16}$$

From the signal acquired with 2D measurements, it is possible to observe how the photoexcitation process acts on photocarriers and phonons response by retrieving the transient change in refracting index and conductivity and comparing this data with the one acquired with a static measure.

2.4.3. Data analysis

To obtain the frequency-dependent complex transmission of the sample, two different acquisitions are needed: one with the sample and a reference. An important aspect is that the acquired traces are in the time domain and give the response of the sample with respect to the instantaneous THz field. The complex transmission in the frequency domain comes easily by performing the ratio of the Fourier transform of the sample and reference electric fields. To extract the complex refractive index, an *exact* method is based on the development of a theoretical model for light propagation inside the medium, finding the expected electric field in the frequency domain after the interaction with the material:

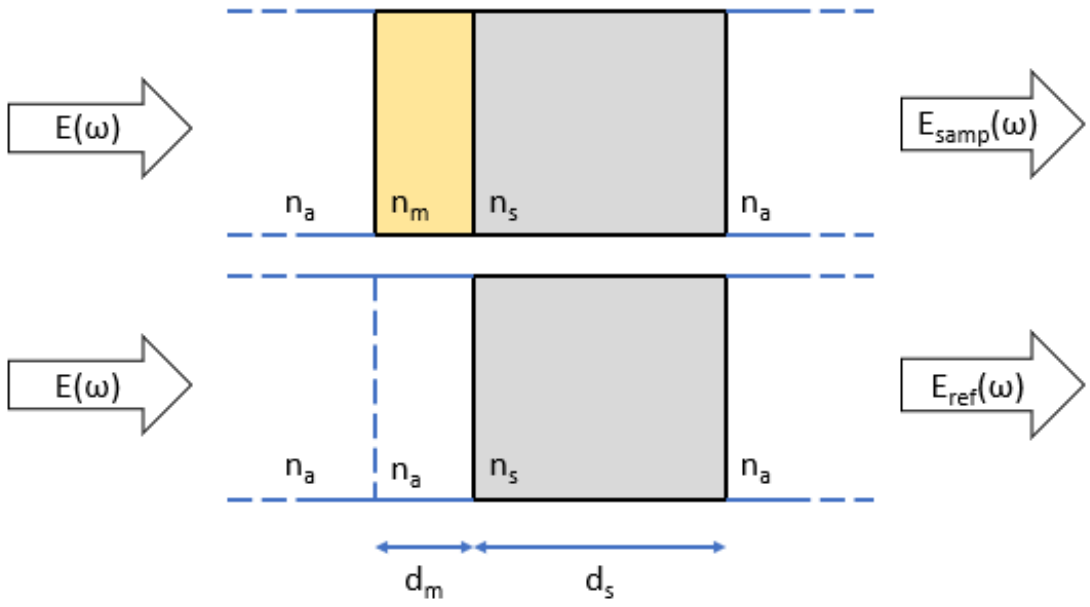

Figure 2.6: Propagation of THz field with and without sample

$$E_{samp}(\omega) = t_{am} e^{id_m k_0 n} FP_{ams} t_{ms} e^{id_s k_0 n_s} FP_{msa} t_{sa} E(\omega) \tag{2.17}$$

Where

$$t_{ab} = \frac{2n_a}{n_a + n_b} \tag{2.18}$$

represents the transmission coefficient from medium a to medium b while n_a is the complex refracting index of the medium a and d_a the thickness of the layer of material a. The exponential represents the propagation term in the medium and $E(\omega)$ is the electric field before the interaction with the sample. Finally FP_{xay} account for the Fabry-Perrot term in the medium a, in between medium x and y which can be modeled as follow:

$$FP_{xay} = \sum_{p=0}^{\infty} \left(r_{ay} r_{ax} e^{2id_a k_0 n_a}\right)^p = \frac{1}{1 - \left(r_{ay} r_{ax} e^{2id_a k_0 n_a}\right)} \tag{2.19}$$

Where $r_{ax} = \frac{n_a - n_x}{n_a + n_x}$ is the reflection coefficient at the a-x interface. The actual structure of the sample is shown in figure 2.6 and it is possible to see that the THz wave propagates first from air to the sample, then from the sample to the substrate and finally from the substrate to the air again. Now it is possible also to derive the reference signal without the sample:

$$E_{ref}(\omega) = e^{id_m k_0 n_a} t_{as} e^{id_s k_0 n_s} t_{sa} FP_{msa} E(\omega) \tag{2.20}$$

In this case, is important to keep the propagation over the distance d_m which is now in the air rather than in the sample to allow the two electric fields to be comparable.

From these two terms is then possible to evaluate the complex transmission of the sample by performing the ratio of the two quantities:

$$T(\omega) = \frac{E_{samp}(\omega)}{E_{ref}(\omega)} = \frac{t_{am} t_{ms}}{t_{as}} e^{id_m k_0 (n_m - n_a)} FP_{ams} \tag{2.21}$$

The only unknown term from this equation is the complex refractive index of the sample n_m. In order to find it we need now to perform an optimization problem to find the best value of n_m that minimize the difference between the experimental transmission $T_{exp}(\omega) = \frac{E_{exp\ samp}(\omega)}{E_{exp\ ref}(\omega)}$ and the theoretical one derived from the physical model just presented $T(\omega)$.

Duvillaret et al. [37] proposed a method to evaluate this root finding problem without requirements on the starting value of n_m by defining the error function as follows:

$$\delta(n_m) = \delta\rho^2 + \delta\varphi^2 \tag{2.22}$$

with

$$\delta\rho = ln(|T(\omega)|) - ln(|T_{exp}(\omega)|)$$
$$\delta\varphi = arg(T(\omega)) - arg(T_{exp}(\omega))$$

The resulting function resembles a paraboloid and allows us to retrieve the value of the complex refractive index by an iterative numerical computation made, for example, with a MATLAB code [37].

From the refractive index we can then retrieve the dielectric function:

$$\epsilon_{stat} = \epsilon' + i\epsilon'' = n_m^2 = (n'_m + in''_m)^2 = ({n'_m}^2 - {n''_m}^2) + 2in'_m n''_m \tag{2.23}$$

and then also the static conductivity of the sample:

$$\sigma_{stat} = -i\omega\epsilon_0\epsilon_{stat} \tag{2.24}$$

Thin film approximation

The numerical evaluation of such a problem requires some amount of computational power. A commonly used solution to this issue is the application of an approximate formula for the derivation of the complex conductivity of a sample starting from the experimental transmission:

$$\sigma(\omega) = \frac{n_s + 1}{Z_0 d_m}\left(\frac{1}{T_{exp}(\omega)} - 1\right) \tag{2.25}$$

Where $Z_0 \simeq 377\,\Omega$ impedance of free space, n_s refracting index of the substrate, and d_m thickness of the sample. This formula was first derived by Glover and Tinkham in 1957 for the evaluation of conductivity of superconductive thin films in the far infrared region, but since then it has gained great importance for its applicability in THz spectroscopy. The requirement needed to be allowed to apply such approximation are:

$$n'_m k_0 d_m \ll 1$$
$$n''_m k_0 d_m \ll 1$$

With n'_m real part of the refracting index and n''_m extinction coefficient [38]. This re-

quirement ought to be checked carefully as a material with higher dielectric constant or resonances may not fall under thin film applicability conditions. Also, it seems that for a low conductivity medium there can be issues with the correct evaluation of the imaginary part of the conductivity[39].

The derivation of this approximation can be understood following the steps performed by Thoman et al. in [40]. By modeling light propagating in the layered sample like an electric signal in a transmission line, it is possible to see the different layers as impedances from which the signal can be transmitted or reflected. This impedance will be in the form:

$$Z = \frac{E}{H} = \frac{Z_0}{n} \tag{2.26}$$

with n refracting index of the layer. The electric field will induce a surface current density in the thin film $j = E\sigma$ that can be assumed constant in the film due to its small thickness. Therefore, we can write:

$$Z_{film} = \frac{E}{H_1 - H_2} \approx \frac{E}{J} = \frac{1}{\sigma d} \tag{2.27}$$

with H_1 and H_2 magnetic field at the boundaries of the film and d thickness of it. The effect of thin film plus substrate can be considered as a parallel of impedance in series with the air surrounding the sample. It is then possible to derive the transmission and reflection coefficient for the structure comprehending the thin film:

$$t = \frac{2Z_s}{Z_s + Z_1} = \frac{2n_1}{n_1 + n_2 + Z_0\sigma d} \tag{2.28}$$

$$r = \frac{Z_s - Z_1}{Z_s + Z_1} = \frac{n_1 - n_2 - Z_0\sigma d}{n_1 + n_2 + Z_0\sigma d} \tag{2.29}$$

where Z_1 impedance of the first medium, air in our case, $Z_s = \left(\frac{1}{Z_2} + \frac{1}{Z_{film}}\right)^{-1}$ impedance of the sample, film Z_{film} plus substrate Z_2. Supposing now that the film thickness approaches zero the previous coefficient will become the common Fresnel coefficient that can be found in section 2.4.3. To retrieve the complex conductivity of the film, as already said, is then necessary to perform the ratio of the electric field Fourier transform with and without the film from which it is possible to get:

$$\frac{E_{samp}}{E_{ref}} = \frac{t}{t_0} = \frac{n_1 + n_2}{n_1 + n_2 + Z_0\sigma(\omega)d} \tag{2.30}$$

obtained by substituting equations 2.28 as t and 2.18 as t_0. It is then easy to invert the equation finding the Tinkham approximation as in equation 2.25, supposing $n_1 = 1$.

3 | Results

In this chapter, the results of the measurements performed on the sample will be presented starting with a brief introduction to the sample itself. MoS_2 belongs to the family of transition metal dichalcogenides (TMDs) and has gained great importance in optics and in electronics thanks to its peculiar properties. The specific sample analyzed in this thesis is a liquid-exfoliated tri-layer of MoS_2. The whole deposition process has been performed three times resulting in a thicker layer of MoS_2 flakes. The thickness of a single trilayer flake is around 2 nm [3], so the total deposited material should be in the range of 6 nm of thickness after the three depositions. Despite the multiple processes, analysis of the sample showed that this deposition technique did not result in the formation of a 9-layer sheet of MoS_2. This effect results from the impossibility of controlling the position and orientation of MoS_2 flakes which, as a result, do not merge in a uniform multilayer structure. Lastly, this deposition technique does not allow for precise control over the actual number of layers in each flake, which is only centered around the three-layer value. The deposition was performed on half of a 2x2 cm, 1 mm-thick fused silica substrate. The choice of this material for the substrate has been made given its high transmittance over the THz bandwidth and also because of its availability with respect to other materials.

Substrate characterization

As the previous chapter presents, a static measurement is performed by varying the time delay between THz and gate pulses. In such a way, exploiting the electro-optic sampling, it is possible to reconstruct the shape in amplitude and phase of the THz pulse after the interaction with the given material. Figure 3.1a shows the data acquired with no sample in the experimental chamber and represents an example of the shape of the actual electric field impinging on the detection crystal. This acquisition, like all the others presented from now on, is performed in a nitrogen-rich atmosphere as the presence of water introduces unwanted absorption in the THz band. The field is nearly a single optical cycle and is thus the shortest possible pulse achievable with ZnTe spectral capabilities. By performing the Fourier transform of this data is then possible to derive the spectral shape of the pulse and becomes clear from figure 3.1b that the available bandwidth in our setup spans roughly

between 0.5 THz and 2 THz.

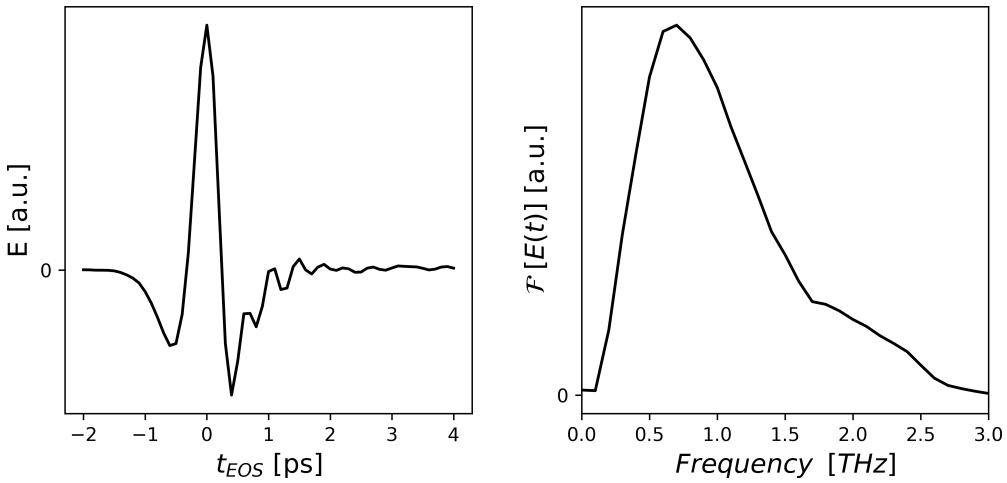

(a) (b)

Figure 3.1: (a) THz electric field detected with EOS in a N_2 rich atmosphere without sample. (b) Spectrum of the THz pulse.

It is pretty common to study samples deposited on substrates as it is not always possible to obtain a free-standing material that can be easily placed in the experimental chamber. For this reason, it is important to work with substrate materials as much transparent as possible to the THz bandwidth in use. The substrates used for the experiments of this thesis are made of fused silica. Before making the presented measurements a characterization of these substrates has been carried out in order to assess the overall quality of the material. First, we studied the static behavior of the substrate to extract its refractive index. The refractive index has been evaluated from an optimization procedure between the experimentally evaluated complex transmission and a physical model regarding the propagation of light inside the media. The acquired THz electric field appears in figure 3.2a where both reference, acquired without any sample at all, and substrate trace are shown. In figure 3.2b we can see the evaluated spectra of the THz pulses.

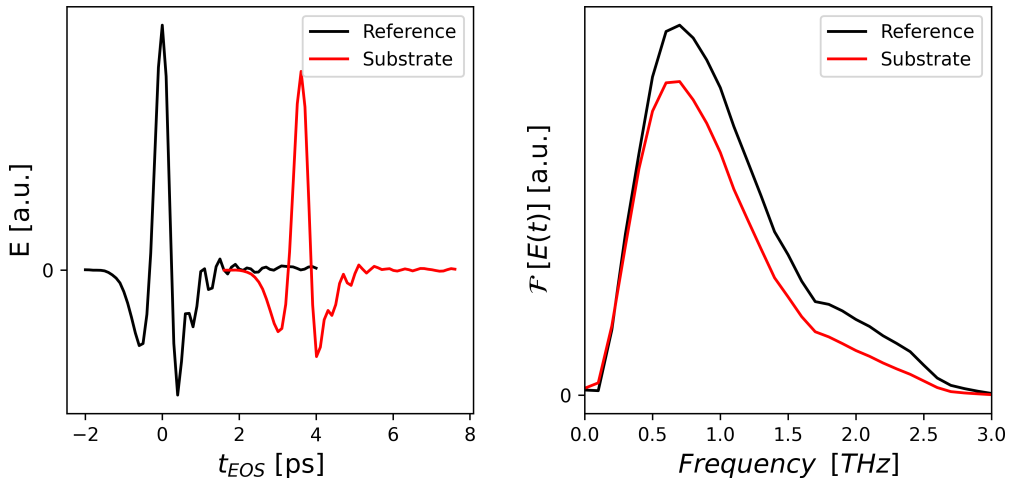

(a) (b)

Figure 3.2: (a) Electric fields and (b) spectra of the THz pulse for the substrate characterization

From these data, we retrieved the complex transmission of the fused silica substrate summarized in figure 3.3. We can see that the substrate does not present particular features in the transmission plot due to the lack of resonances in the sample.

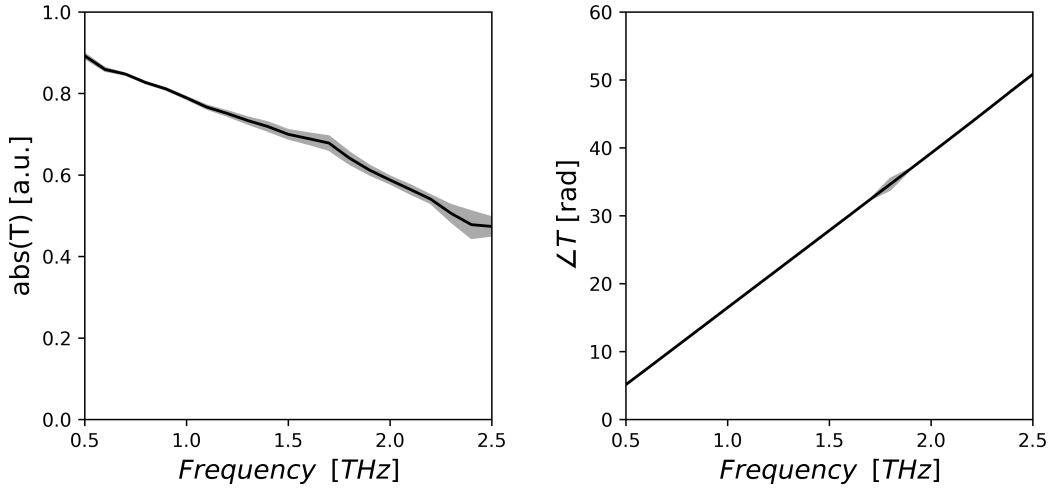

(a) (b)

Figure 3.3: (a)Absolute value and (b) phase of the complex transmission of the fused silica substrate

After the optimization procedure based also in this case on the loss function defined in 2.22, we found the refractive index presented in figure 3.4. The value of the extinction

coefficient, linked with the absorption coefficient, is very small, as this substrate presents very low absorption in the THz bandwidth exploited in the experiments.

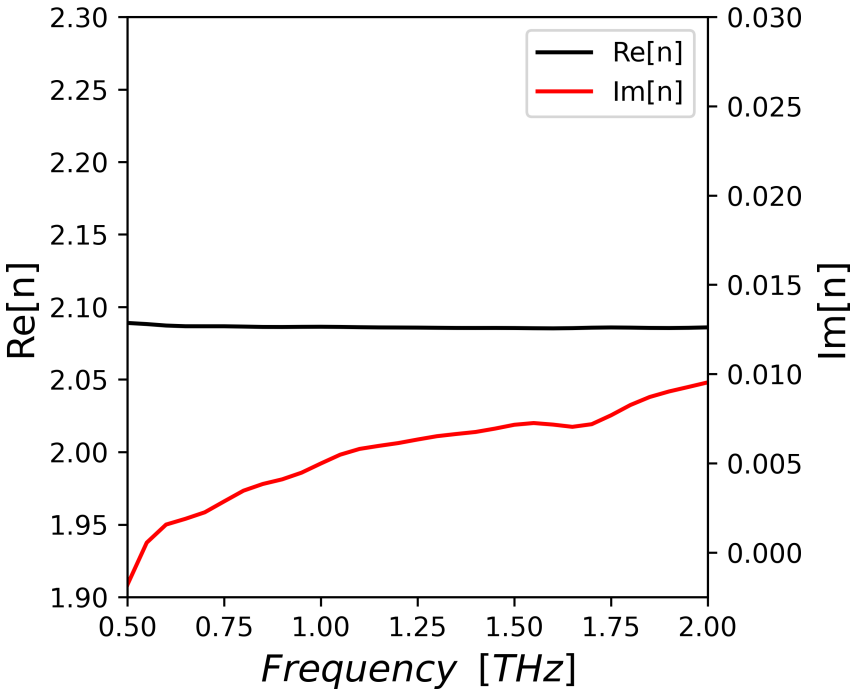

Figure 3.4: Refractive index of the fused silica substrate

3.1. Static measurments

The acquisitions needed for the static analysis of MoS_2 are shown in figure 3.5 where both electric field and spectrum are displayed for both the substrate and the sample.

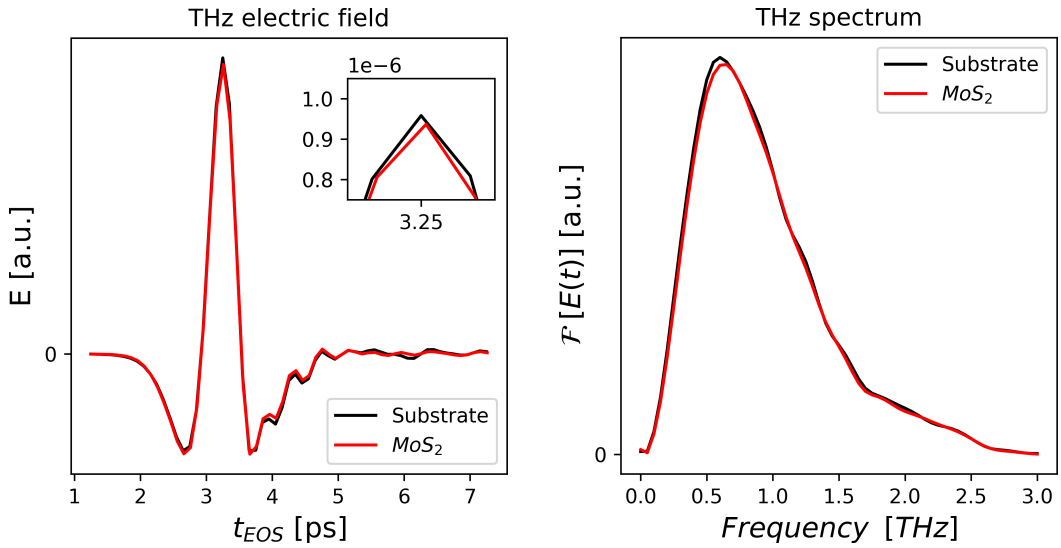

(a) (b)

Figure 3.5: (a) Electric field and (b) spectrum of THz pulse, on MoS_2 and substrate

By performing the ratio of the spectra of the THz pulses we can evaluate the experimentally measured complex transmission of the MoS_2 sample, which can be seen in figure 3.6.

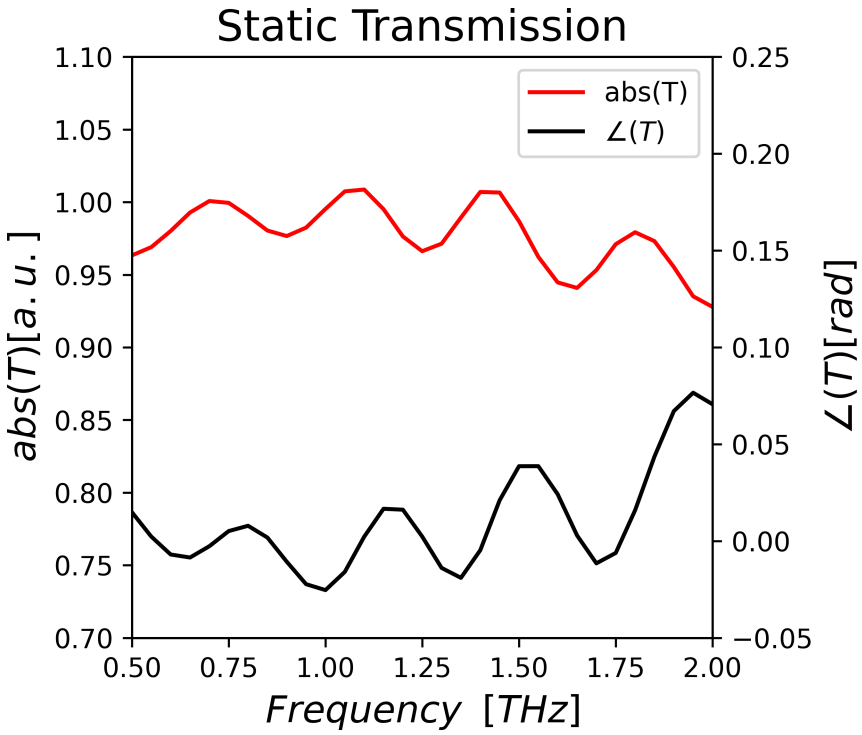

Figure 3.6: Static complex transmission of MoS_2 , absolute value and phase

From previous observations on these kinds of substrates, we discovered that there can be variations in thickness even across the same substrate which are impossible to know before the measurements. Given the very high precision of the THz measurement, these imperfections are clearly noticeable and need to be corrected before following with the data analysis. In order to do so, it is necessary to add a propagation term in the transmission model found in equation 2.4.3 to account for the missing thin layer of fused silica, obtaining:

$$T_{corrected}(\omega) = T(\omega)e^{idLk_0(n_s - n_a)} \tag{3.1}$$

with an added thickness of $dL = 2\,\mu m$. This value of dL was chosen to get a MoS_2 refracting index closer to the value obtained in the literature as in [41].

The corrected theoretical model was then slightly simplified by eliminating the Fabry-Perot term. This term accounts for the multiple reflections of light inside a specific material, which arises replicas of the incident pulse shifted in time according to the thickness of the sample itself. In the case presented in this thesis, the sample is composed of roughly nine layers of MoS_2 for a total thickness centered around 6 nm. As a consequence, we do not expect to observe any Fabry-Perot replicas as they would be overlapped with the main first pulse. Because of this, equation 2.21 can be rewritten discarding the FP_{ams}, by adding then the correction of equation 3.1 we obtain:

$$T(\omega) = \frac{E_{samp}(\omega)}{E_{ref}(\omega)} = \frac{t_{am}t_{ms}}{t_{as}} e^{id_m k_0(n_m - n_a)} e^{idLk_0(n_s - n_a)} \tag{3.2}$$

Now, with the introduced corrections it is possible to solve the minimization problem given by 2.22, evaluating the complex refractive index of the sample of MoS_2 , which is shown in figure 3.7.

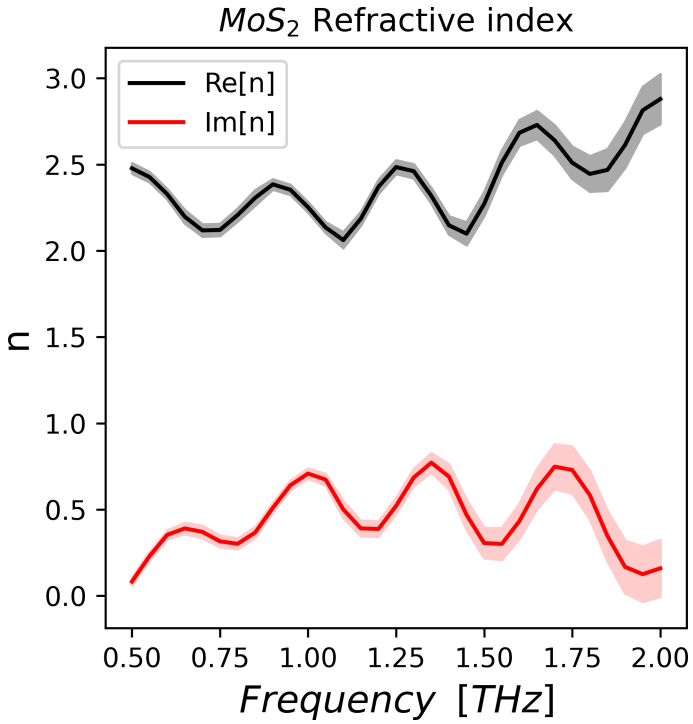

Figure 3.7: Complex refractive index of MoS_2 . With real part in black and extinction coefficient in red. The shaded regions represent the error bars of the presented values

The complex conductivity can then be derived from this information by applying equation 2.24 together with 2.23 obtaining the result shown in figure 3.8.

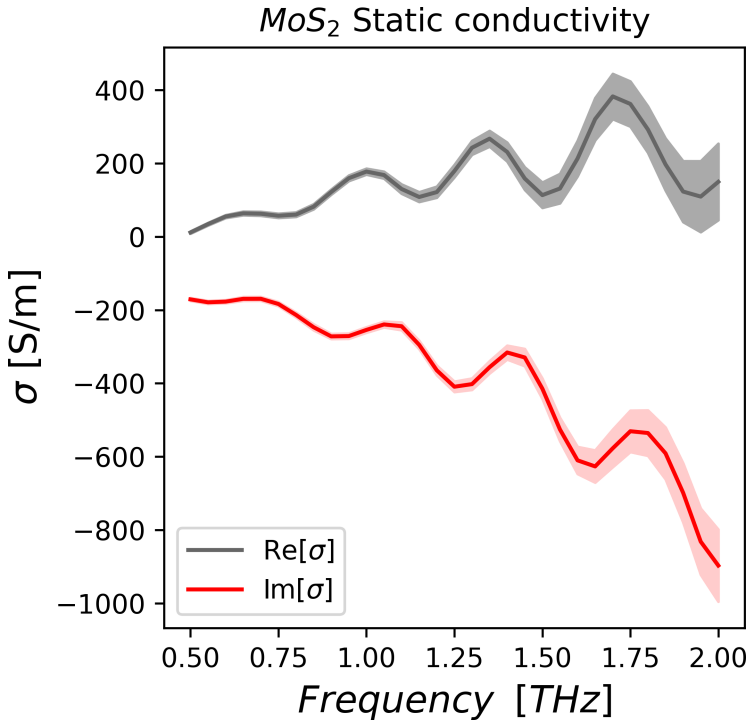

Figure 3.8: Complex static conductivity of MoS_2 . With real part in black and imaginary part in red. Error bars showed with the shaded regions

The next step is to fit the experimental conductivity with a suitable function from which it is then possible to determine the physical phenomena involved in the photoexcitation of layered MoS_2 .

The simplest response arising from the presence of free carriers goes under the name of Drude response and can be derived from the description of the motion of a charge inside a solid. The resulting conductivity is:

$$\sigma_D(\omega) = \frac{\sigma_{DC}}{1 - i\omega\tau} \tag{3.3}$$

where σ_{DC} is the DC conductivity of the material and τ is the scattering time of the charge carriers. Supposing that long-rage carriers' transport is suppressed by the presence of grain and boundaries in the structure of the sample, it is possible to apply a correction to the Drude formula to account for the backscattering of carriers. The resulting model comes under the name of Drude-Smith model:

$$\sigma_{DS}(\omega) = \frac{\epsilon_0 \omega_p^2 \tau}{1 - i\omega\tau}\left(1 + \frac{c}{1 - i\omega\tau}\right) \tag{3.4}$$

where ω_p is the plasma frequency of the material, τ is the scattering time and c is a constant accounting for the backscattering process.

The THz field is able to interact also with resonances arising from fundamental excitations and collective modes like phonons inside the materials. A description of the response of such resonances involves the Lorentz oscillator model from which it is possible to derive a generalization of the Drude model with the addition of a Lorentzian resonance centered at a finite frequency [42]. The Lorentzian resonance can be described as:

$$\sigma_{DL} = \frac{gf}{i(f_0^2 - f^2) + \Gamma f} \tag{3.5}$$

where g represents the amplitude of the Lorentzian, resonance centered at frequency f_0, and with damping factor given by Γ.

To fit the observed behavior of the static conductivity it was necessary to suppose the presence of five different resonances with the fifth one at higher frequencies with respect to the observed region, together with a Drude-Smith term. The result of the fit are shown in figure 3.9 and the extrapolated parameters of the Lorentzian are summarized in table 3.1.

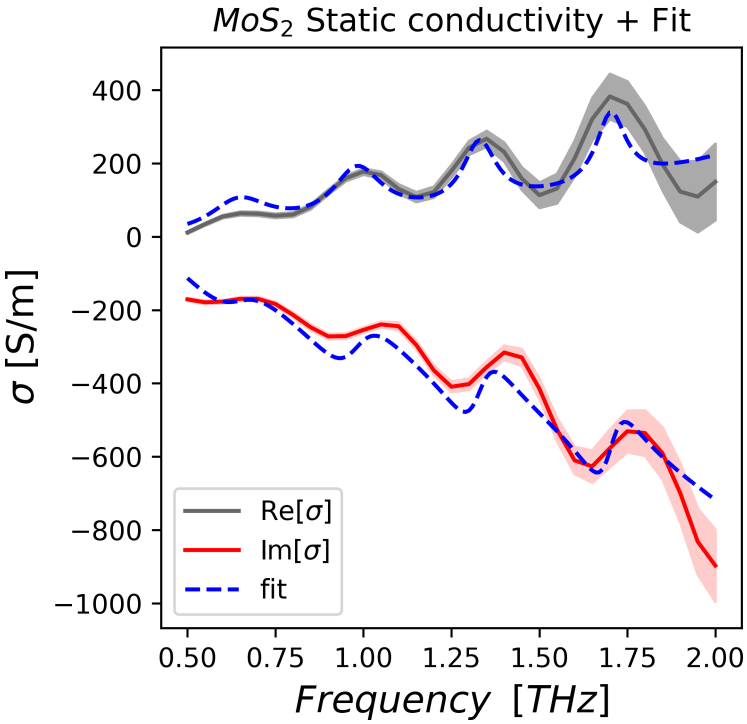

Figure 3.9: Result of the fit of the complex conductivity of MoS_2 , with the fit represented by blue dashed lines. The shaded regions are error bars representing the variability of the data. The Shaded regions represent the error bar of the conductivity.

	L1	L2	L3	L4	L5
g $[Sm^{-3}ps^{-1}]$	17.5	24	20	19.5	6900
f_0 [THz]	0.64	0.98	1.32	1.70	4.43
Γ [THz]	0.20	0.17	0.11	0.10	2

Table 3.1: Lorentzian parameters extrapolated from the static conductivity fit of MoS_2

Multilayer MoS_2 samples are expected to be lightly n-doped [16], therefore the Drude-Smith response can be attributed to the presence of free carriers in the sample. On top of this, layered MoS_2 presents some IR active vibrational modes at lower frequencies in the form of shear and breathing oscillations of the layers, where shear vibrations involve the sliding of a layer on top of another while breathing modes suppose an oscillation in the orthogonal direction. These modes have been observed in [17] with Raman spectroscopy but there is yet no observation with THz time-domain spectroscopy. Pizzi et al. in [43] presented an online tool that helps with the evaluation of the frequency position and type of these vibrational modes. To perform the calculation it was necessary to define the force constant of the two vibrational modes for MoS_2. Zhao et al. in [17] obtained with a fitting procedure the value of these constants: $K_x = 2.72 \cdot 10^{19} Nm^{-3}$ and $K_z = 8.62 \cdot 10^{19} Nm^{-3}$. The resulting modes are presented in figure 3.10.

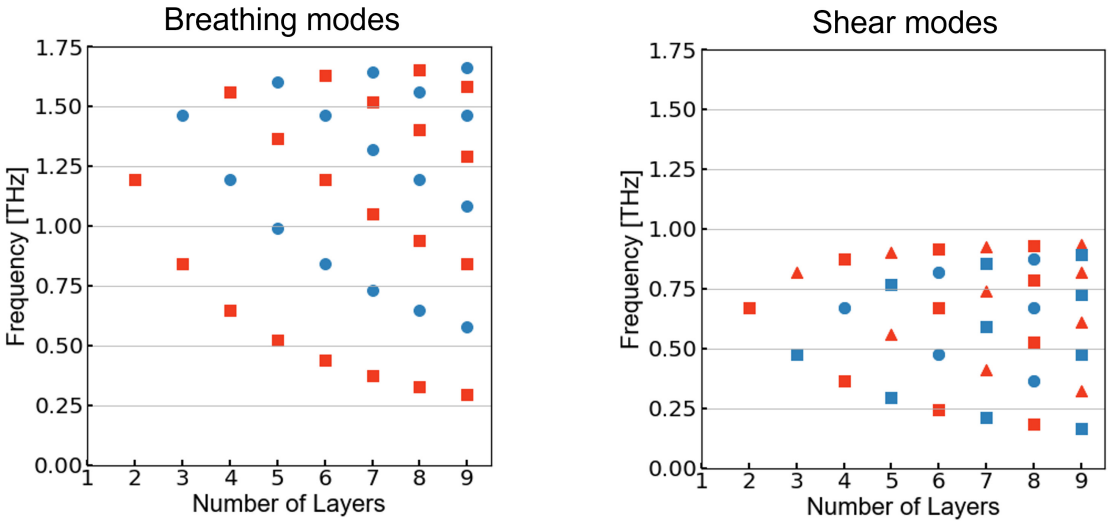

(a) (b)

Figure 3.10: (a) Breathing and (b) shear modes in MoS_2 evaluated by a tool proposed by Pizzi et al. [43]. Blue circle for IR active modes, red square and blue square for Raman active modes, red triangles for both Raman and IR active modes.

From figure 3.10 we can see that shear modes live under 1 THz while breathing modes go up to 1.75 THz for a multiple layers configuration.

The THz field impinging on the sample is linearly polarized, parallel to the plane of the layers. Supposing that the layers of MoS_2 are perpendicularly stacked we would expect to be able to observe only shear mode as the field would not be able to excite breathing ones. However, there was no particular control during the deposition of the layers, therefore we could expect to be able to excite also the latter supposing that the geometry of the deposited flakes is not perfectly plane. Moreover, the layers distribution is not uniform and only centered around the three-layer so it is not possible to exclude the possibility of observing modes arising from a higher or lower layer distribution.

Given these assumptions on MoS_2 , we expect that the first four Lorentzian resonances obtained with the fit correspond with shear and breathing modes as they are all under the 1.75 THz limit, while the fifth resonance can be interpreted as a trion resonance as found in [44].

3.2. Pump-probe measurements

We will now present the data acquired with pump-probe measurement. The pump pulse used in this case had photons at 400 nm with an energy of around 3 eV; since the indirect band-gap of trilayer MoS_2 is at around 1.29 eV, the excitation energy was above the band-gap.

Regarding the choice of the fluences for the following experiments, Wang et al. in [45] stated that their MoS_2 monolayer sample got permanently damaged when performing irradiation with pump pulses with fluence above 50 $\mu J\, cm^{-2}$. Measurements performed on the damaged sample showed a radical change in the measured transient response with longer time scales. Two of the fluences taken into account for these experiments are actually over this proposed damage threshold. However, there is no direct observation of a change in the dynamics at this fluence rate with respect to prior data acquisition. We must take into consideration that Wang's work was about monolayer MoS_2 while in our case the sample was a triple deposition of MoS_2 trilayers, and this could explain this discrepancy.

3.2.1. 1D Dynamic

In a 1D dynamic measurement, we perform a pump-probe experiment without scanning the full THz wave, focusing only on specific points of the electric field. The results of this acquisition allow for the retrieval of the frequency averaged response of the photoconductivity which can then be interpreted depending on which point we are actually choosing for the THz wave. By fixing the wave on its peak we expect to probe the interaction with the highest possible value of the THz electric field, this point is more sensitive to amplitude variation and is less affected by phase variation of the field. This amplitude variation comes from the low-frequency interaction of the field with the photoexcited free carriers and thus its dynamic can be traced to the real conductive response of the sample. Another peculiar point of interest is the zero crossing point, where the electric field crosses the zero value changing sign. This point, on the other hand, is more sensitive to phase shift and less to amplitude changes and can be linked with the shape of the imaginary part of the photoconductivity [46]. In this experiment, we performed only measurements on the peak of the THz pulse as the signal-to-noise ratio was far too low to extrapolate information about the interaction with the zero crossing point of the pulse. The measurements have been performed at the following fluences: 95.5 $\mu J\, cm^{-2}$, 70 $\mu J\, cm^{-2}$, 48.3 $\mu J\, cm^{-2}$, and are shown together in figure 3.11.

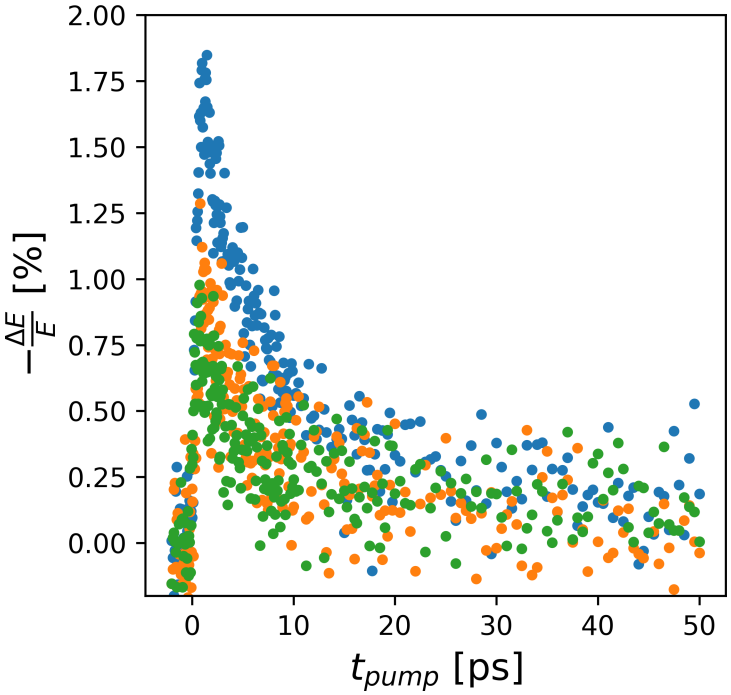

Figure 3.11: 1D dynamics measurements at the fluences of: (blue) 95.5 $\mu J\, cm^{-2}$, (orange) 70 $\mu J\, cm^{-2}$, (green) 48.3 $\mu J\, cm^{-2}$

The signals presented in figure 3.11 are characterized by a formation time of about 1 ps comparable with the impulse response function of the setup, for this reason, we can consider this formation as instantaneous. After this, we can observe the maximum intensity of the signal, followed by a decay that lasts for about 50 ps after which the signal is approximately zero.

Following the decay dynamics of the signal, it is possible to infer the decay mechanism governing MoS_2, which determines the relaxation of the charge carriers excited by the pump pulse. The main processes involved in carrier relaxation in layered MoS_2 are dominated by defect-assisted recombination, which determines the capture of electrons and holes mainly by two mechanisms: Auger processes and phonon-assisted processes. These Auger processes are mainly due to the strong Coulomb interaction and electron-hole correlation typical of two-dimensional metal dichalcogenides [45]. In particular, Wang et al. observed that the temperature independence of the recombination dynamics could be linked mainly to Auger recombination processes [16].

Several experiments showed how the fitting of MoS_2 relaxation dynamics could be divided into two different exponentials determined by different time scales [47][16][48]. To explain this behavior, Wang et al. proposed in [45] the existence of two different types of defects, for instance, fast and slow traps. It is known that monolayer MoS_2 present different kinds

of possible defects and thus it is possible to infer that some of these traps inside the band gap determine recombination at different rates. On the other hand, Strait et al. in [47] supposed the existence of a single type of trap, explaining the two different time scales by supposing a saturation of these recombination centers which effectively slows down the whole relaxation process.

Following these previous results, the equation chosen for the fitting of the normalized relaxation dynamics is a double exponential in the form of:

$$y(t) = A_1 e^{\frac{-t}{\tau_1}} + (1 - A_1) e^{\frac{-t}{\tau_2}} \tag{3.6}$$

Where y(t) are the normalized dynamics, τ_1 and τ_2 are the characteristic times of the two exponentials, and A_n their amplitudes.

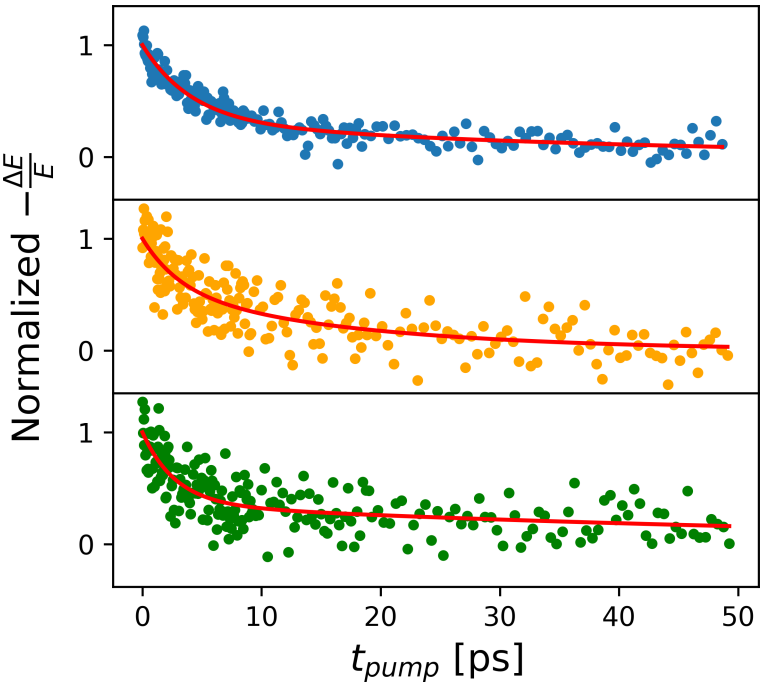

Figure 3.12: Fit of MoS_2 dynamics at the fluences of: (blue) 95.5 $\mu J\, cm^{-2}$, (orange) 70 $\mu J\, cm^{-2}$, (green) 48.3 $\mu J\, cm^{-2}$

The fitting produced the result showed in figure 3.12 with the parameters summarized in table 3.2.

Fluence $[\mu J\, cm^{-2}]$	A_1	τ_1 [ps]	$(1 - A_1)$	τ_2 [ps]
48.3	0.6	2.7	0.4	62.1
70	0.4	3.1	0.6	17.6
95.5	0.7	4.1	0.3	38.4

Table 3.2: Parameters extrapolated from the fits of MoS_2 dynamics recorded at the peak of the THz pulse

Considering then the confidence intervals of the previously presented parameters, there is no direct observation of a fluence dependence, and the difference between the measures can be attributed to the decrease in signal-to-noise ratio at lower fluence rates. Comparing the obtained decay rates with the one proposed in the literature as in [16] it appears that the fast capture rate is similar while the slower one is smaller that the one retrieved by Wang, which is in the order of 100 ps for the trilayer and increasing with the number of layers. These results were explained by supposing that recombination centers are mainly found on the surface of the MoS_2 structure thus a multi-layer structure presented less of these surface defect states. In our case, the faster slow recombination rate could be explained by supposing an abundance of point defects in the sample together with the effect of electron-phonon coupling coming from the observed vibrational modes. Moreover, the work of Wang et al. was sensitive to both exciton and free carriers while the signal here obtained arises only from free carriers and interaction with the vibrational modes, so a difference in the resulting decay rate is expected.

Another piece of information we can extrapolate from 1D dynamics measurement is the mobility of photoexcited charge carriers. An electromagnetic field impinging on a material can get reflected, transmitted, or absorbed. This latter contribution is the one responsible for the formation of free charges in the sample. For energy conservation purposes, this statement can be summarized by the following relation:

$$R + T + Abs = 1 \tag{3.7}$$

Where R, T, and Abs are respectively the reflectance, the transmittance, and the absorbed fraction of the sample. By rewriting the transmittance in terms of optical density, OD, it is possible to obtain the following expression for the absorbed fraction of light by a medium:

$$Abs = (1 - R)(1 - 10^{-OD}) \tag{3.8}$$

From this equation is trivial to obtain the number of absorbed photons:

$$N_{ph} = \frac{E}{h\nu} Abs = \frac{E}{h\nu}(1-R)(1-10^{-OD}) \tag{3.9}$$

with E pulse energy. Not all absorbed photons end up exciting a charge carrier, for this reason, it is commonly introduced [49] an efficiency term ϕ as the photon-to-charge branching ratio obtaining the initial number of photoexcited carriers:

$$N_0 = \phi\frac{E}{h\nu} Abs = \phi\frac{E}{h\nu}(1-R)(1-10^{-OD}) \tag{3.10}$$

Following the derivation of charge carrier mobility proposed in [49] we have that:

$$\mu = \frac{\Delta S A_{eff}}{Ne} \tag{3.11}$$

Where $\Delta S = -\epsilon_0 c(n_a + n_b)\left(\frac{\Delta T}{T}\right)$ is the sheet photoconductivity of a thin film in between media n_a and n_b, A_{eff} effective area of interaction of the pump, N_0 initial number of photoexcited carriers and e elementary charge. We are interested in the charge mobility at the maximum value of $\frac{\Delta T}{T} \propto \frac{\Delta E}{E}$ which is the value we obtain with the acquisition. By plugging 3.10 into 3.11 we can finally get:

$$\phi\mu = \epsilon_0 c\frac{n_a + n_b}{e}\frac{A_{eff}}{E}\frac{h\nu}{(1-R)(1-10^{-OD})}\left(\frac{-\Delta E}{E}\right) \tag{3.12}$$

Since the value of ϕ is unknown the measurement allows only for the retrieval of $\widetilde{\mu} = \phi\mu$ The value of ϕ spans between 0 and 1 so that the evaluated mobility is just a lower limit of the real value. To get the value of the mobility we require now the evaluation of the optical density of our specific sample of MoS_2 . The absorbance of the sample has been measured during its fabrication with a spectrophotometer. In such a way it is then possible to retrieve the amount of light absorbed at a specific wavelength. With a scan over the visible region, it was possible to get the data shown in figure 3.13 from which we get that the optical density of our sample is roughly 0.5.

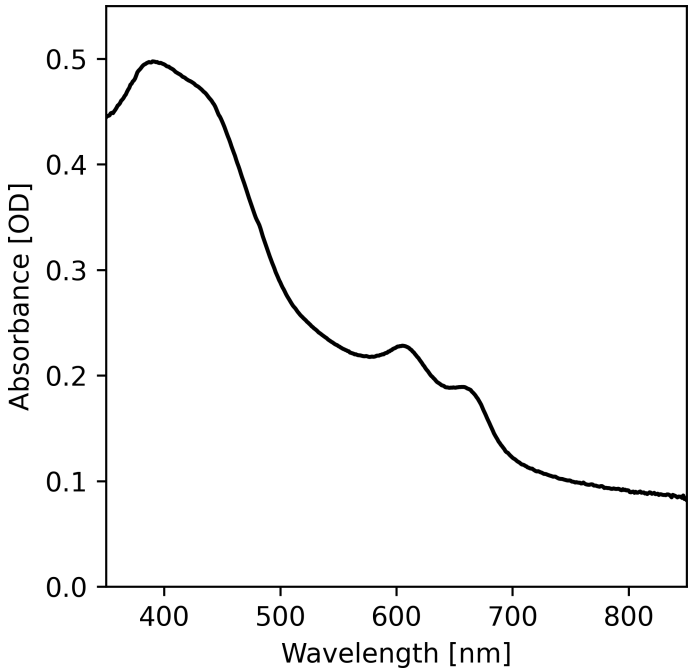

Figure 3.13: Optical density of the MoS_2 sample measured with a spectrophotometer

Supposing now to set R=0 neglecting the amount of radiation reflected by the sample, we can evaluate an estimation of the charge carriers' mobility inside the sample of MoS_2 . The results are shown in table 3.3 together with the density of photoexcited charge carriers in the material.

Fluence $[\mu J\, cm^{-2}]$	n_{ph} $[\cdot 10^{20}\, cm^{-3}]$	$\phi\mu$ $[cm^2\,(V\,s)^{-1}]$
48.3	1.11	5.74
70	1.6	4.55
95.5	2.19	6.78

Table 3.3: Photoexcited charge density and mobility evaluated at three fluences starting from dynamic measurements

These values of charge carriers' mobility are way lower than the value obtained by Strait et al. in [47], where mobility in the order of $257 \pm 30\, cm^2\,(V\,s)^{-1}$ has been found at room temperature. They suggest that the dominant mobility limiting factor depends on impurity and defect scattering. Following the observation of the slow decay rate presented for 1D dynamics, it could be possible that the supposed higher number of defects originates from a reduction in the value of charge carriers' mobility. Grain boundaries and defects arising from the actual structure of the sample could so be the reason for the observed value of mobility. Considering also the observation of vibrational resonances is possible

to infer that the coupling between phonons and charges plays a role in the limitation of charges' mobility.

3.2.2. 2D Maps

The 2D pump-probe experiment was performed at increasing fluences. The measured signal represents the relative change in the transmission of the sample after photoexcitation at different time delays determined by t_{pump}. Given the data obtained out of the setup, the complex relative variation of the transmission can be evaluated with equation 2.16. In figure 3.14 it is possible to observe three different maps regarding the differential electric field at the fluences of 48.3, 70, and 95.5 $\mu J\, cm^{-2}$. The greater change in the electric field is around the peak of the pulse and we can see as t_{pump} evolve that the induced change is slowly dumping.

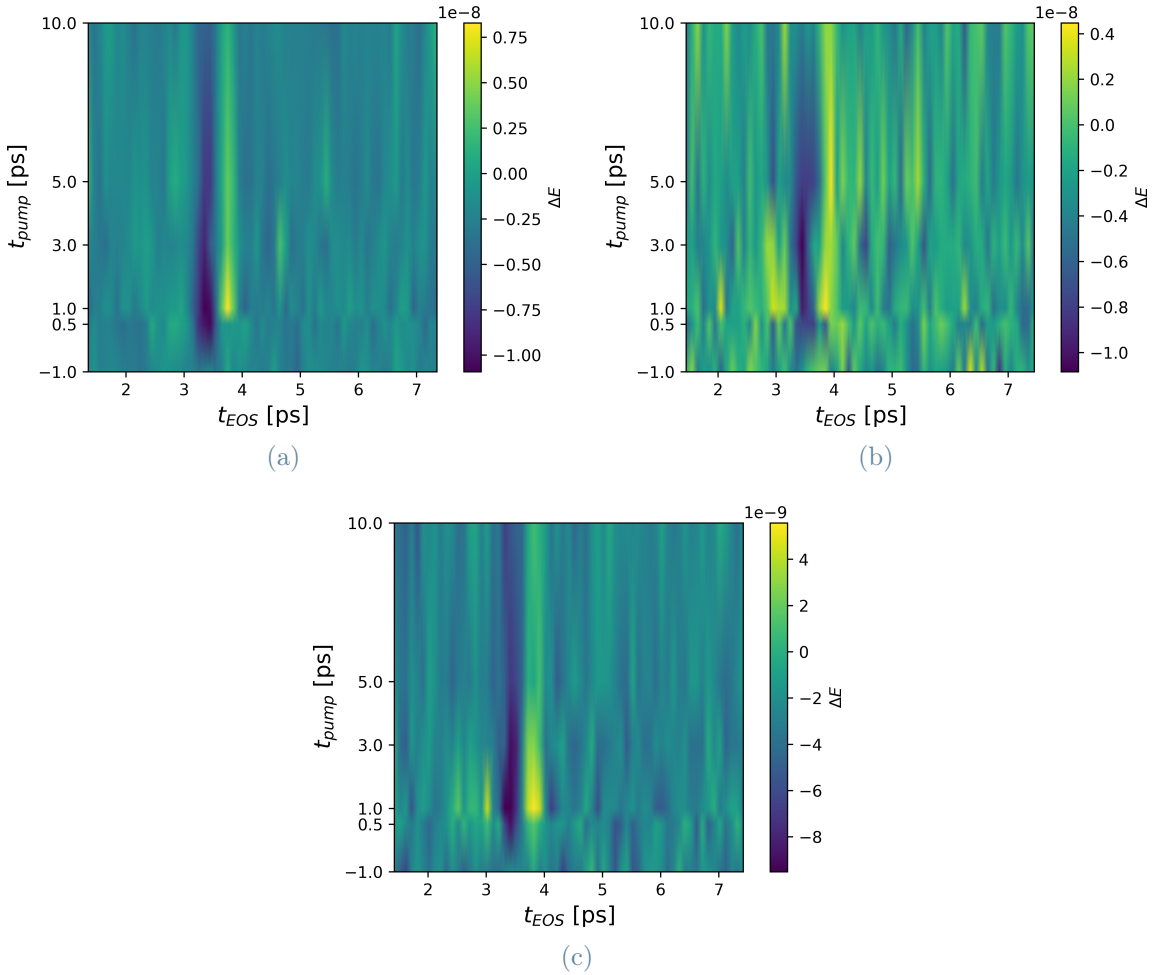

Figure 3.14: 2D plot of the change in electric field with respect to the pump-off case at the fluences of (a) 95.5 $\mu J\, cm^{-2}$, (b) 70 $\mu J\, cm^{-2}$, (c) 48.3 $\mu J\, cm^{-2}$

By choosing then the desired pump-probe delay we can apply the same process presented for static measurement in order to retrieve the photoexcited refractive index of the sample. In this case, the acquisition is performed on the same spot of the material for the pump-on and pump-off conditions, in order to neglect differences in substrate thickness. The physical model for transmission accounts only for the change in optical properties between the pump-on and pump-off conditions. The transmission is then:

$$T(\omega) = \frac{t_{ap}t_{ps}}{t_{am}t_{ms}} e^{idk_0(n_p - n_m)} \tag{3.13}$$

Where t_{ab} is the Fresnel transmission coefficient between medium a and b and the subscripts represent respectively a, air, p, photoexcited material, m, non-photoexcited material, and s, substrate. The optimization procedure is performed again with the loss function defined by 2.22 and, as a result, it is possible to retrieve the complex variation of the refractive index of MoS_2 . Following the same procedure adopted before, it is then possible to obtain first the differential dielectric function via 2.23 and then, with 2.24 we can finally find the differential complex conductivity due to the photoexcitation.

To fit the resulting transient photoconductivity it is first necessary to concentrate on a specific pump-probe delay. In this case, the choice was to perform the fitting at a pump-probe delay of 1 ps, as dynamics measurements showed that this delay corresponds to the higher signal achievable. In figure 3.15 we can observe the theoretical fit performed with the same method proposed in [50] by Zhao et al. The fit function was there obtained supposing small pump-induced changes by differentiating the static fit's formula. For each Lorentzian, the differentiation involved changes both in amplitude and in center frequency, as the damping rate seems to remain constant from the gathered data. The fit formula for a single Lorentzian is then:

$$d\sigma(f) = \frac{f}{i(f_0^2 - f^2) + \Gamma f} dg + \frac{-2if_0 gf}{[i(f_0^2 - f^2) + \Gamma f]^2} df_0 \tag{3.14}$$

Where the value of g, f_0 and Γ are the ones derived before with the static conductivity fit. The results of the fit are shown in figure 3.15 at the three fluences proposed before with the extrapolated parameters summarised in table 3.4.

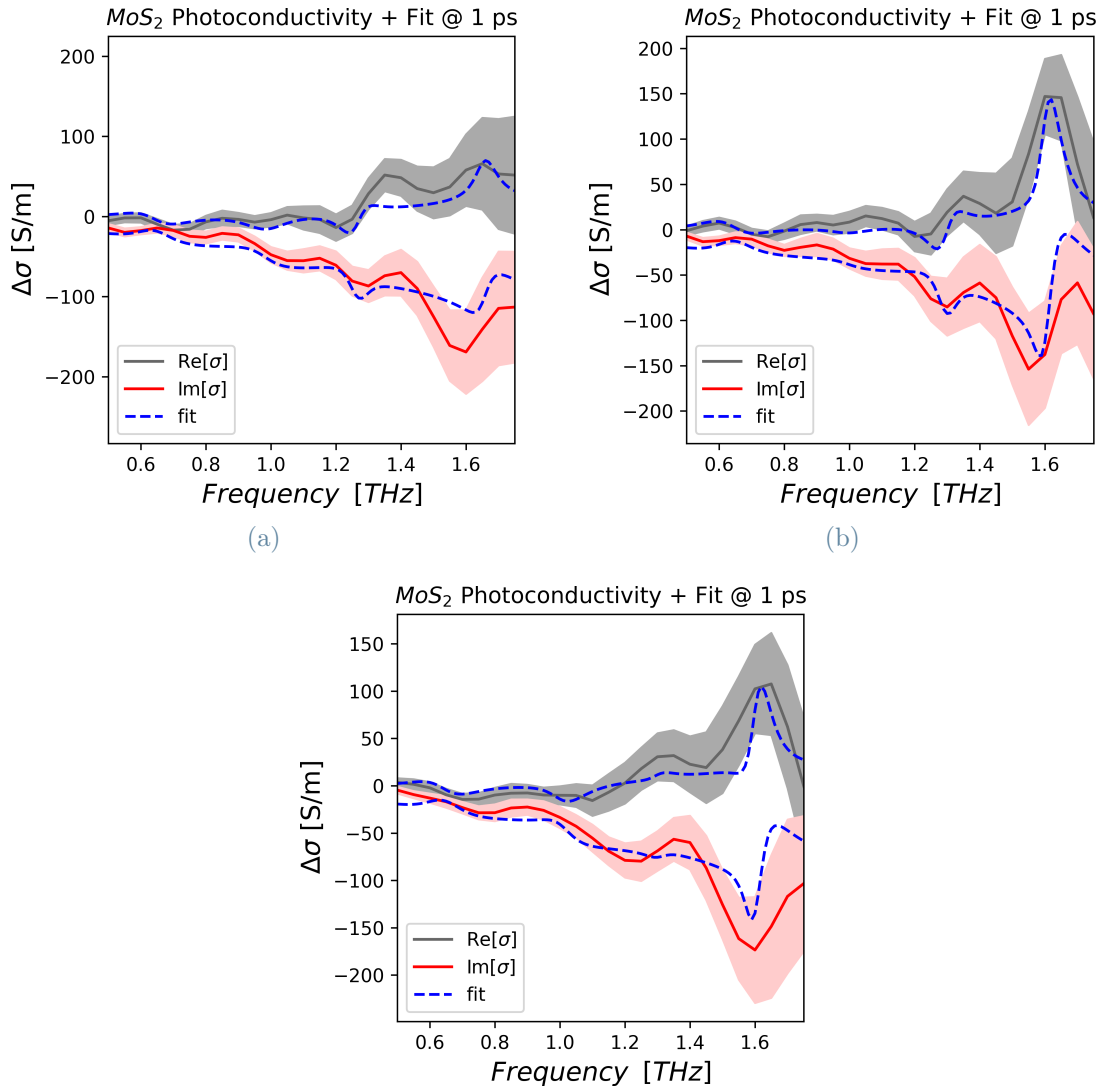

Figure 3.15: Plot of the differential photoconductivity induced at a fixed $t_{pump} = 1\,ps$ with the evaluated fit at the following fluences: (a) 95.5 $\mu J\,cm^{-2}$, (b) 70 $\mu J\,cm^{-2}$, (c) 48.3 $\mu J\,cm^{-2}$

In this case, there is no direct observation of a Drude-Smith behavior, and the obtained data presents features arising from the pump-induced interactions with the vibrational modes presented before.

Fluence	L1		L2		L3		L4		L5	
$\mu J\, cm^{-2}$	dg	df_0	dg	df_0	dg	df_0	dg	df_0	dg	df_0
48.3	-1.15	-0.01	-3.1	-0.004	0.54	0.001	6.5	0.01	800	0
70	0.19	-0.01	-1.1	0	-1.27	0.01	11	0.01	650	0
95.5	-1.24	-0.01	-3.2	0	-1.6	0.01	5	0.004	946	0

Table 3.4: Parameters extrapolated from the photoconductivity fit of MoS_2

The relative change in the center frequency of the fifth Lorentzian has been manually set to 0 while its amplitude increase could be interpreted as an increment in the trion population due to the pump influence. It does not appear a clear pattern in the variation of both amplitude and frequency with the presented measure. This pump-induced response could be linked with a coupling between the low-frequency vibrational modes and charge carriers, with a consequential limitation of the mobility of these carriers [51].

The difficulty in finding a possible trend upon photoexcitation can be linked to the structure of the sample itself. By looking directly at the sample in figure 3.16 it is clear that the distribution of the material is not completely homogeneous. For this reason, it is possible that upon subsequent measures performed on different days the probed area on the sample was slightly different with a corresponding different flakes distribution which could lead to discrepancies when comparing multiple data acquisitions.

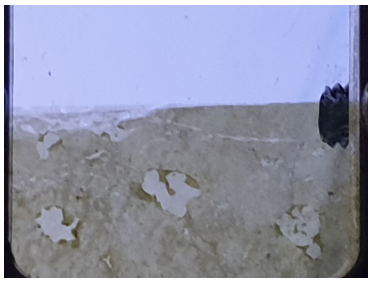

Figure 3.16: Photo of the actual sample of MoS_2 studied in this thesis. MoS_2 on the bottom and fused silica substrate on the top

4 | Conclusions

In conclusion, this thesis presented several time-resolved THz spectroscopy experiments performed on a sample of MoS_2 concentrating on the changes induced by the interaction of the material with a pump pulse at 400 nm at three different fluences: 95.5 $\mu J\, cm^{-2}$, 70 $\mu J\, cm^{-2}$, 48.3 $\mu J\, cm^{-2}$. The choice of these fluence values resulted from the necessity of being able to observe a signal arising over the noise level with the possibility of observing a trend linked with the number of photons impinging on the sample.

The static measurements showed the presence of features in the conductivity of MoS_2 which did not vanish with the increasing number of measures mediated. Zhao et al, showed the presence of low-frequency IR active modes due to breathing and shear motion between the layer of the atomic structure with resonances in the frequency band observable with our THz setup. The observed resonances do not perfectly match with a particular distribution of layers but all lie under the threshold value of 1.75 THz presented as the limit frequencies for breathing modes. This impossibility to link the trilayer modeled modes with the observed resonances could be linked to the distribution of layers deposited during the liquid exfoliation performed for the preparation of the sample. There is no direct measure of the number of layers of the flakes deposited which can then vary around the trilayer with a certain statistical distribution. On top of that, the deposition process has been performed three times thus generating an even more complex distribution of layered flakes. During the fit of the static conductivity, it was also necessary to suppose the presence of an unobservable resonance out of the explored bandwidth which could be linked with the presence of a trion at higher frequencies interacting with its tail with the vibrational modes. Trion presence has been observed in both monolayer and multilayer MoS_2 [52][53].

Pump-probe measurements were then performed to study how these modes interacted after the excitation of the sample by a pump pulse at 400 nm. The resulting dynamics of the transient photoconductivity actually showed a transient change in transmission of our sample that can be linked to the coupling between charges and phonons inside the material. Supposing a small variation of the features observed in the static measure, a

new fitting model presented in [49] was used. From the parameters extrapolated from the fitting procedure at three different fluences values, it is not possible to state that there is an actual trend in the change of amplitude and central frequency of the vibrational modes.

Lastly, dynamics measures were fitted with a bi-exponential function accounting for the presence of both fast and slow recombination centers due to defects in the MoS_2 structure. These defects seem to be mainly distributed on the surfaces of the sample, for this reason increasing the number of layers on the sample decrease the slow trap decay rate with a longer relaxation dynamics. The results of the fit showed that the faster recombination rate was comparable with the value determined in other studies such as [16], while the slower recombination rate was linked, in our case, with a faster decay rate with respect to literature. This effect could be linked with the presence of more defects in the sample studied with respect to the one exploited in other experiments presented in the other papers. Nonetheless, by following the results of the 2D pump-probe measure performed, it is also possible to link this faster decay rate with the coupling of charge carriers with the phonons of the low-frequency vibrational mode. This same effect could then be responsible for the lower mobility derived from the dynamics measures.

To further develop the topics presented in this thesis it is first necessary to improve the signal-to-noise ratio of the THz setup. To do so, it would be necessary to improve the optimization of the optical elements exploited in the setup, especially regarding the THz parabolas and their configuration. An increment in THz bandwidth would also be a good improvement to allow the acquisition of data with a bigger spectral range. In this way, it would be possible to investigate the presence and position of the fifth resonance needed in the fitting of the static conductivity which was associated with the presence of a trion. To do so, it could be possible to change the THz generation and detection crystal shifting for example from ZnTe to GaP. By performing such improvements it would then be possible to acquire less noisy signals, allowing also to explore the response of the material at lower fluences rates with respect to the ones presented and to study weaker signals typically given by few-layer samples of 2D materials. Another possible development could also be the analysis of samples fabricated with different techniques, like chemical vapor deposition or mechanical exfoliation to investigate how the use of different techniques could also be reflected in the properties of the resulting sample.

Bibliography

[1] K. S. Novoselov, A. K. Geim, S. V. Morozov, D. Jiang, Y. Zhang, S. V. Dubonos, I. V. Grigorieva, and A. A. Firsov, "Electric field effect in atomically thin carbon films," *Science*, vol. 306, pp. 666–669, 10 2004.

[2] X. Leng, S. Chen, K. Yang, M. Chen, M. Shaker, E. E. Vdovin, Q. Ge, K. S. Novoselov, and D. V. Andreeva, *Introduction to Two-Dimensional Materials*. WORLD SCIENTIFIC, 11 2021.

[3] V. Nicolosi, M. Chhowalla, M. G. Kanatzidis, M. S. Strano, and J. N. Coleman, "Liquid exfoliation of layered materials," *Science*, vol. 340, 6 2013.

[4] B. Radisavljevic, A. Radenovic, J. Brivio, V. Giacometti, and A. Kis, "Single-layer mos2 transistors," *Nature Nanotechnology*, vol. 6, pp. 147–150, 3 2011.

[5] S. Bertolazzi, P. Bondavalli, S. Roche, T. San, S.-Y. Choi, L. Colombo, F. Bonaccorso, and P. Samorì, "Nonvolatile memories based on graphene and related 2d materials," *Advanced Materials*, vol. 31, p. 1806663, 3 2019.

[6] Q. Zeng and Z. Liu, "Novel optoelectronic devices: Transition-metal-dichalcogenide-based 2d heterostructures," *Advanced Electronic Materials*, vol. 4, p. 1700335, 2 2018.

[7] W. Zheng, Y. Jiang, X. Hu, H. Li, Z. Zeng, X. Wang, and A. Pan, "Light emission properties of 2d transition metal dichalcogenides: Fundamentals and applications," *Advanced Optical Materials*, vol. 6, p. 1800420, 11 2018.

[8] Z. Wang, D. Sapkota, T. Taniguchi, K. Watanabe, D. Mandrus, and A. F. Morpurgo, "Tunneling spin valves based on fe3 gete2 /hbn/fe3 gete2 van der waals heterostructures," *Nano Letters*, vol. 18, pp. 4303–4308, 7 2018.

[9] R. G. Dickinson and L. Pauling, "The crystal structure of molybdenite," *Journal of the American Chemical Society*, vol. 45, pp. 1466–1471, 6 1923.

[10] P. Joensen, R. Frindt, and S. Morrison, "Single-layer mos2," *Materials Research Bulletin*, vol. 21, pp. 457–461, 4 1986.

[11] K. F. Mak, C. Lee, J. Hone, J. Shan, and T. F. Heinz, "Atomically thin mos2: A new direct-gap semiconductor," *Physical Review Letters*, vol. 105, p. 136805, 9 2010.

[12] M. M. Ugeda, A. J. Bradley, S.-F. Shi, F. H. da Jornada, Y. Zhang, D. Y. Qiu, W. Ruan, S.-K. Mo, Z. Hussain, Z.-X. Shen, F. Wang, S. G. Louie, and M. F. Crommie, "Giant bandgap renormalization and excitonic effects in a monolayer transition metal dichalcogenide semiconductor," *Nature Materials*, vol. 13, pp. 1091–1095, 12 2014.

[13] K. F. Mak, K. He, C. Lee, G. H. Lee, J. Hone, T. F. Heinz, and J. Shan, "Tightly bound trions in monolayer mos2," *Nature Materials*, vol. 12, pp. 207–211, 3 2013.

[14] P. Jepsen, D. Cooke, and M. Koch, "Terahertz spectroscopy and imaging - modern techniques and applications," *Laser I& Photonics Reviews*, vol. 5, pp. 124–166, 1 2011.

[15] F. Wang, J. Shan, M. A. Islam, I. P. Herman, M. Bonn, and T. F. Heinz, "Exciton polarizability in semiconductor nanocrystals," *Nature Materials*, vol. 5, pp. 861–864, 11 2006.

[16] H. Wang, C. Zhang, and F. Rana, "Surface recombination limited lifetimes of photoexcited carriers in few-layer transition metal dichalcogenide mos2," *Nano Letters*, vol. 15, pp. 8204–8210, 12 2015.

[17] Y. Zhao, X. Luo, H. Li, J. Zhang, P. T. Araujo, C. K. Gan, J. Wu, H. Zhang, S. Y. Quek, M. S. Dresselhaus, and Q. Xiong, "Interlayer breathing and shear modes in few-trilayer mos2 and wse2," *Nano Letters*, vol. 13, pp. 1007–1015, 3 2013.

[18] J. Neu and C. A. Schmuttenmaer, "Tutorial: An introduction to terahertz time domain spectroscopy (thz-tds)," *Journal of Applied Physics*, vol. 124, 12 2018.

[19] Y.-S. Lee, *Principles of Terahertz Science and Technology*. Springer US, 2009.

[20] N. M. Burford and M. O. El-Shenawee, "Review of terahertz photoconductive antenna technology," *Optical Engineering*, vol. 56, p. 010901, 1 2017.

[21] M. C. Nuss and J. Orenstein, *Terahertz time-domain spectroscopy*, vol. 74. Springer Berlin Heidelberg, 1998.

[22] F. Zernike and P. R. Berman, "Generation of far infrared as a difference frequency," *Physical Review Letters*, vol. 15, pp. 999–1001, 12 1965.

[23] I. Wilke and S. Sengupta, *Nonlinear Optical Techniques for Terahertz Pulse Genera-*

tion and Detection - Optical Rectification and Electrooptic Sampling. CRC Press, 12 2007.

[24] K. Reimann, "Table-top sources of ultrashort thz pulses," *Reports on Progress in Physics*, vol. 70, pp. 1597–1632, 10 2007.

[25] K. Aoki, J. Savolainen, and M. Havenith, "Broadband terahertz pulse generation by optical rectification in gap crystals," *Applied Physics Letters*, vol. 110, p. 201103, 5 2017.

[26] M. Ashida, "Ultra-broadband terahertz wave detection using photoconductive antenna," *Japanese Journal of Applied Physics*, vol. 47, pp. 8221–8225, 10 2008.

[27] I. Katayama, R. Akai, M. Bito, E. Matsubara, and M. Ashida, "Electric field detection of phase-locked near-infrared pulses using photoconductive antenna," *Optics Express*, vol. 21, p. 16248, 7 2013.

[28] J. A. Spies, J. Neu, U. T. Tayvah, M. D. Capobianco, B. Pattengale, S. Ostresh, and C. A. Schmuttenmaer, "Terahertz spectroscopy of emerging materials," *The Journal of Physical Chemistry C*, vol. 124, pp. 22335–22346, 10 2020.

[29] D. J. Cook and R. M. Hochstrasser, "Intense terahertz pulses by four-wave rectification in air," *Optics Letters*, vol. 25, p. 1210, 8 2000.

[30] K.-Y. Kim, J. H. Glownia, A. J. Taylor, and G. Rodriguez, "Terahertz emission from ultrafast ionizing air in symmetry-broken laser fields," *Optics Express*, vol. 15, p. 4577, 2007.

[31] E. Matsubara, M. Nagai, and M. Ashida, "Coherent infrared spectroscopy system from terahertz to near infrared using air plasma produced by 10-fs pulses," *Journal of the Optical Society of America B*, vol. 30, p. 1627, 6 2013.

[32] F. Sizov, "Thz radiation sensors," *Opto-Electronics Review*, vol. 18, 1 2010.

[33] G. Gallot and D. Grischkowsky, "Electro-optic detection of terahertz radiation," *Journal of the Optical Society of America B*, vol. 16, p. 1204, 8 1999.

[34] D. N. Erschens, D. Turchinovich, and P. U. Jepsen, "Nonlinear generation and detection of thz pulses in znte with chirped femtosecond laser pulses," pp. 1–1, IEEE, 9 2010.

[35] Z. Instruments, "Principles of lock-in detection and the state of the art," 2016.

[36] K. Iwaszczuk, D. G. Cooke, M. Fujiwara, H. Hashimoto, and P. U. Jepsen, "Simul-

taneous reference and differential waveform acquisition in time-resolved terahertz spectroscopy," *Optics Express*, vol. 17, p. 21969, 11 2009.

[37] L. Duvillaret, F. Garet, and J. L. Coutaz, "A reliable method for extraction of material parameters in terahertz time-domain spectroscopy," *IEEE Journal on Selected Topics in Quantum Electronics*, vol. 2, pp. 739–745, 9 1996.

[38] J. Neu, K. P. Regan, J. R. Swierk, and C. A. Schmuttenmaer, "Applicability of the thin-film approximation in terahertz photoconductivity measurements," *Applied Physics Letters*, vol. 113, 12 2018.

[39] J. Lloyd-Hughes and T.-I. Jeon, "A review of the terahertz conductivity of bulk and nano-materials," *Journal of Infrared, Millimeter, and Terahertz Waves*, vol. 33, pp. 871–925, 9 2012.

[40] A. Thoman, A. Kern, H. Helm, and M. Walther, "Nanostructured gold films as broadband terahertz antireflection coatings," *Physical Review B - Condensed Matter and Materials Physics*, vol. 77, 5 2008.

[41] X. Yan, L. Zhu, Y. Zhou, Y. E, L. Wang, and X. Xu, "Dielectric property of mos2 crystal in terahertz and visible regions," *Applied Optics*, vol. 54, p. 6732, 8 2015.

[42] R. Ulbricht, E. Hendry, J. Shan, T. F. Heinz, and M. Bonn, "Carrier dynamics in semiconductors studied with time-resolved terahertz spectroscopy," *Reviews of Modern Physics*, vol. 83, pp. 543–586, 6 2011.

[43] G. Pizzi, S. Milana, A. C. Ferrari, N. Marzari, and M. Gibertini, "Shear and breathing modes of layered materials," *ACS Nano*, vol. 15, pp. 12509–12534, 8 2021.

[44] C. J. Docherty, P. Parkinson, H. J. Joyce, M. H. Chiu, C. H. Chen, M. Y. Lee, L. J. Li, L. M. Herz, and M. B. Johnston, "Ultrafast transient terahertz conductivity of monolayer mos2and wse2 grown by chemical vapor deposition," *ACS Nano*, vol. 8, pp. 11147–11153, 11 2014.

[45] H. Wang, C. Zhang, and F. Rana, "Ultrafast dynamics of defect-assisted electron-hole recombination in monolayer mos2," *Nano Letters*, vol. 15, pp. 339–345, 1 2015.

[46] P. D. Cunningham, "Accessing terahertz complex conductivity dynamics in the time-domain," *IEEE Transactions on Terahertz Science and Technology*, vol. 3, pp. 494–498, 2013.

[47] J. H. Strait, P. Nene, and F. Rana, "High intrinsic mobility and ultrafast carrier

dynamics in multilayer metal-dichalcogenide mos2," *Physical Review B - Condensed Matter and Materials Physics*, vol. 90, 12 2014.

[48] S. Kar, Y. Su, R. R. Nair, and A. K. Sood, "Probing photoexcited carriers in a few-layer mos2 laminate by time-resolved optical pump–terahertz probe spectroscopy," *ACS Nano*, vol. 9, pp. 12004–12010, 12 2015.

[49] C. Wehrenfennig, G. E. Eperon, M. B. Johnston, H. J. Snaith, and L. M. Herz, "High charge carrier mobilities and lifetimes in organolead trihalide perovskites," *Advanced Materials*, vol. 26, pp. 1584–1589, 3 2014.

[50] D. Zhao, H. Hu, R. Haselsberger, R. A. Marcus, M.-E. Michel-Beyerle, Y. M. Lam, J.-X. Zhu, C. L. o vorakiat, M. C. Beard, and E. E. M. Chia, "Monitoring electron–phonon interactions in lead halide perovskites using time-resolved thz spectroscopy," *ACS Nano*, vol. 13, pp. 8826–8835, 8 2019.

[51] K. Kaasbjerg, K. S. Thygesen, and K. W. Jacobsen, "Phonon-limited mobility in n-type single-layer mos2 from first principles," *Physical Review B*, vol. 85, p. 115317, 3 2012.

[52] J. Pei, J. Yang, R. Xu, Y.-H. Zeng, Y. W. Myint, S. Zhang, J.-C. Zheng, Q. Qin, X. Wang, W. Jiang, and Y. Lu, "Exciton and trion dynamics in bilayer mos2," *Small*, vol. 11, pp. 6384–6390, 12 2015.

[53] S. Golovynskyi, I. Irfan, M. Bosi, L. Seravalli, O. I. Datsenko, I. Golovynska, B. Li, D. Lin, and J. Qu, "Exciton and trion in few-layer mos2: Thickness- and temperature-dependent photoluminescence," *Applied Surface Science*, vol. 515, p. 146033, 6 2020.

List of Figures

List of Tables

Ringraziamenti

Vorrei ora spendere due parole per ringraziare coloro che mi hanno aiutato e supportato durante questo percorso.

Innanzitutto vorrei ringraziare il professore Salvatore Stagira, assieme a Eugenio Cinquanta e Caterina Vozzi per tutto l'aiuto e i consigli e l'aiuto datomi in questo periodo di tesi. Ringrazio anche tutti i ragazzi e ragazze del laboratorio Udyni e soprattutto Lorenzo per l'infinita pazienza verso uno sprovveduto che non aveva quasi mai visto un laser dal vivo. Ovviamente un profondo ringraziamento anche alla mia famiglia per avermi supportato durante tutto questo percorso anche nei momenti più difficili. Un grazie infinito a Gio, che mi ha sopportato nelle mie ansie e timori, come nei miei discorsi sconclusionati senza né capo né coda; senza di te sarebbe stato tutto decisamente più difficile. Ed infine un grazie a tutti i miei cari amici che in tutti questi anni sono stati al mio fianco a condividere gioie e tristezze. Posso solo dirmi fortunato ad aver trovato in questi anni persone come voi.